Tectonophysics 833 (2022) 229353

Contents lists available at ScienceDirect

Tectonophysics

journal homepage: www.elsevier.com/locate/tecto

3D imaging of the subsurface electrical resistivity structure in West Bohemia/Upper Palatinate covering mofettes and Quaternary volcanic structures by using Magnetotellurics

Anna Platz [a,*], Ute Weckmann [a,b], Josef Pek [c], Světlana Kováčiková [c], Radek Klanica [c], Johannes Mair [a,d], Basel Aleid [a,b]

[a] GFZ German Research Centre for Geosciences, Potsdam, Germany
[b] University of Potsdam, Institute of Earth and Environmental Science, Potsdam, Germany
[c] Institute of Geophysics of the Czech Academy of Sciences, Prague, Czech Republic
[d] Freie Universität Berlin, Department of Earth Sciences, Berlin, Germany

ARTICLE INFO

Keywords:
Magnetotellurics
Ohře Rift
Conductive channel
Fluid/magma reservoir
Earthquake swarm

ABSTRACT

The region of West Bohemia and Upper Palatinate belongs to the West Bohemian Massif. The study area is situated at the junction of three different Variscan tectonic units and hosts the ENE-WSW trending Ohře Rift as well as many different fault systems. The entire region is characterized by ongoing magmatic processes in the intra-continental lithospheric mantle expressed by a series of phenomena, including e.g. the occurrence of repeated earthquake swarms and massive degassing of mantle derived CO_2 in form of mineral springs and mofettes. Ongoing active tectonics is mainly manifested by Cenozoic volcanism represented by different Quaternary volcanic structures. All these phenomena make the Ohře Rift a unique target area for European intra-continental geo-scientific research. With magnetotelluric (MT) measurements we image the subsurface distribution of the electrical resistivity and map possible fluid pathways. Two-dimensional (2D) inversion results by Muñoz et al. (2018) reveal a conductive channel in the vicinity of the earthquake swarm region that extends from the lower crust to the surface forming a pathway for fluids into the region of the mofettes. A second conductive channel is present in the south of their model; however, their 2D inversions allow ambiguous interpretations of this feature. Therefore, we conducted a large 3D MT field experiment extending the study area towards the south. The 3D inversion result matches well with the known geology imaging different fluid/magma reservoirs at crust-mantle depth and mapping possible fluid pathways from the reservoirs to the surface feeding known mofettes and spas. A comparison of 3D and 2D inversion results suggests that the 2D inversion results are considerably characterized by 3D and off-profile structures. In this context, the new results advocate for the swarm earthquakes being located in the resistive host rock surrounding the conductive channels; a finding in line with observations e.g. at the San Andreas Fault, California.

1. Introduction

The cross-border region of West Bohemia and Upper Palatinate between the Czech Republic and Germany belongs to the western part of the Bohemian Massif. The Bohemian Massif developed approximately between 500 and 250 *Ma* during a period of large-scale crustal convergence, subduction, collision of continental plates and microplates as well as post-collisional extension (Matte et al., 1990). Nowadays, this region is situated at the junction of three different Variscan tectonic units and is characterized by the intersection of the ENE-WSW trending Ohře (Eger) Rift and a multitude of different fault systems. The Ohře Rift is part of the seismically active European Cenozoic Rift System and represents its easternmost termination (Ziegler, 1992; Prodehl et al., 2006). The entire area currently shows activity from magmatic processes in the intra-continental lithospheric mantle (e.g Geissler et al., 2005; Bräuer et al., 2009; Muñoz et al., 2018), similar to the Basin and Range Province in the western United States (Jarchow et al., 1993) or the Eifel and the Massif Central in Europe (Ziegler, 1992; Prodehl et al., 1995). These processes take place in the absence of active volcanism at surface, but are expressed by a series of phenomena, including e.g. the

* Corresponding author.
E-mail address: aplatz@gfz-potsdam.de (A. Platz).

https://doi.org/10.1016/j.tecto.2022.229353
Received 17 December 2021; Received in revised form 5 April 2022; Accepted 11 April 2022
Available online 18 April 2022

occurrence of repeated earthquake swarms (e.g. Horálek and Fischer, 2009; Fischer et al., 2014, and references therein) and massive degassing of mantle derived CO_2 in the form of mineral springs and mofettes (e.g. Bräuer et al., 2005, 2008; Kämpf et al., 2013; Weinlich, 2014). Mofettes are sites of natural, cold, magmatogene CO_2 degassing (Flechsig et al., 2008) and can occur as dry as well as wet mofettes. In the latter case, the gas is transported through water close to the surface and the dissolved CO_2 causes an increase of the electrical conductivity within fluids.

Active tectonics in the study area is mainly manifested by Cenozoic volcanism represented by different Quaternary volcanic structures e.g. two scoria cones (Železná and Komorní hůrka) and several maar structures (e.g. Mrlina et al., 2009; Rohrmüller et al., 2018; Mrlina et al., 2019; Hošek et al., 2019) some tens of kilometres away from the zone of earthquake swarms. Based on geo-thermobarometry, a depth range of 25 to 40 km is assumed to be the intrusion level for the alkaline melts in the past and also presently (Geissler et al., 2007). All these phenomena make the Ohře Rift a unique target area for European intra-continental geo-scientific research. Therefore, an interdisciplinary drilling programme advancing the field of earthquake-fluid-rock-biosphere interaction was funded within the scope of the International Continental Scientific Drilling Program (ICDP, Dahm et al., 2013, 2016). This programme continues and expands previous active seismic and passive monitoring experiments as well as magnetotelluric (MT) experiments (e.g. DEKORP Research Group, 1987; Červ et al., 1997a, 1997b; Enderle et al., 1998; Červ et al., 2001; Eisel et al., 2001; Oettinger et al., 2001; Grad et al., 2008; Hrubcová et al., 2013; Mullick et al., 2015) over the last decade to study the crustal and upper mantle structure mainly in the context of the former KTB drilling at Windisch-Eschenbach, Germany (Kontinentale Tiefbohrprogramm der Bundesrepublik Deutschland (KTB); Emmermann and Lauterjung, 1997, and references therein). Since the activities were widespread in the area, the overarching goals were to study (i) the nature of geophysical structures and phenomena, (ii) the crustal stress field and the brittle-ductile transition, (iii) the thermal structure of the crust, (iv) crustal fluids and transport processes, and (v) structure and evolution of the central European Variscan basement. Within the context of the Eger Rift ICDP, a central goal has been the understanding of the physical and chemical processes and interaction that lead to the magma and fluid transport through the lithosphere and crust as well as the processes that lead to the observed earthquake swarms as the cause of all these processes is still enigmatic for an intraplate setting. Several local geo-scientific studies (e.g. Weinlich et al., 1998; Bräuer et al., 2003, 2008; Horálek and Fischer, 2009; Kämpf et al., 2013; Weinlich et al., 2013; Weinlich, 2014; Nickschick et al., 2015) suggest that fluid circulation along deep-reaching faults seems to play a crucial role in explaining the underlying geodynamic processes.

Electromagnetic (EM) methods are suitable to identify and image possible fluid pathways as a strong contrast in electrical resistivity is expected between the resistive crystalline basement and conductive fluids as well as partial melts (e.g. Haak and Hutton, 1986; Simpson and Bahr, 2005; Chave and Jones, 2012). To resolve conductive structures down to the middle crust, the MT method is essential as it is the only EM method capable of reaching such depths. In the past, this method has been applied successfully to image crustal fluids in a variety of geological contexts, like the Tibetan Plateau (Unsworth et al., 2005; Bai et al., 2010), the Japanes back arc (Ogawa et al., 2001, 2014), the Dead Sea (Meqbel et al., 2016), the Barberton Greenstone Belt (Kütter et al., 2016), the San Andreas Fault (Becken et al., 2011) or in different (intraplate) volcanic fields or systems (e.g. Aivazpourporgou et al., 2015; Gao et al., 2020; Comeau et al., 2022). First MT measurements within the ICDP framework were carried out in 2015/2016 along two 50 km long perpendicular profiles with 30 stations each and a dense grid of 97 stations close to the mofettes with an extension of $10\,x\,5\,km^2$. Muñoz et al. (2018) present 2D images along a N-S profile. They reveal a conductive channel at the earthquake swarm region that extends from the lower crust to the surface forming a pathway for fluids into the region of the mofettes. A second conductive channel is present in the south of their model. Due to the given station setup, the resulting 2D inversions allow ambiguous interpretations of this feature. 3D MT data and inversions are required to distinguish between different scenarios and to fully describe the 3D structure of the subsurface. Therefore, we conducted a large MT field experiment in 2018 by extending the study area towards the south. Broad-band (10^{-4} – $10^{3}s$) MT data were measured at 83 stations along three $50 - 75\,km$ long profiles and some additional stations across the region of the maars, the Aš-Tachov fault and the suture zones allowing for 2D as well as 3D inversion on a crustal scale. To improve the data quality, advanced data processing techniques were applied leading to good quality transfer functions. Furthermore, the previously collected MT data were reprocessed using new processing approaches. This entire MT data set across the Ohře Rift environment together with old MT data collected within the framework of the site characterization in the surrounding of the KTB drilling are used to compute a comprehensive 3D resistivity model of the subsurface. The 3D inversion result will be introduced and discussed. Furthermore, 2D inversion studies using real and synthetic data were conducted and the results will be compared to the 3D result.

2. Tectonic and geological setting

2.1. The survey area

The region of West Bohemia and Upper Palatinate at the border between the Czech Republic and Germany (Fig. 1a) belongs to the western part of the Bohemian Massif. The Bohemian Massif is one of the largest stable outcrops of pre-Permian rocks in Central and Western Europe (Matte et al., 1990; Fischer et al., 2014) and is located on the territory of the Czech Republic, Germany, Poland and Austria. The Bohemian Massif was formed during the Variscan cycle resulting from the convergence and collision between two major continents, Laurentia-Baltica-Avalonia and Gondwana with several small microplates, after the closure of various ocean basins, followed by obduction, continental collision, continental subduction, and strike-slip faulting between 500 and 250 Ma (e.g. Hrubcová et al., 2005; Grygar, 2016; Plomerová et al., 2016). It is one of the most significant and extensive fragments of the Variscan orogeny (Matte et al., 1990; Hrubcová et al., 2005; Grygar, 2016). Based on differences in structure and geological evolution, the Bohemian Massif can be divided into (i) the Saxothuringian Unit, (ii) the Teplá-Barrandian Unit, (iii) the Moldanubian Unit and (iv) the Moravo-Silesian Unit (Grygar, 2016).

Northwest Bohemia is located within the transition zone of the first three tectonic units (Fig. 1b) with the Saxothuringian in the north and the Teplá-Barrandian and the Moldanubian unit in the south (Geissler et al., 2005; Bräuer et al., 2014). The different units are separated by significant sutures and fault zones (Grad et al., 2008; Grygar, 2016). Since the Lower Triassic the Paleozoic sutures between the Saxothuringian and the Teplá-Barrandian/Moldanubian units have been reactivated repeatedly as a result of the Alpine collision (Ziegler, 1992; Fischer et al., 2014; Hrubcová et al., 2017).

Prominent tectonic structures of the western part of the Bohemian Massif are the Cenozoic ENE-WSW trending Ohře Rift with the central Ohře Graben, the N-S trending Regensburg-Leipzig-Rostock Zone (RLRZ) and the NNW-SSE trending Cheb–Domažlice Graben (e.g. Bankwitz et al., 2003; Bräuer et al., 2003; Mrlina et al., 2009). Intraplate stress originating in the Alpine collision zone as well as alkaline magmatic activity during the Cenozoic led to the development of the Ohře Rift (Dèzes et al., 2004; Dahm et al., 2013; Fischer et al., 2014). At present times, the Ohře Rift is 300 km long and 70 km wide and is located at the northern border of the Bohemian Massif separating the Saxothuringian and Teplá-Barrandian unit (Bräuer et al., 2003; Geissler et al., 2005; Heuer et al., 2006). The Ohře Rift is the easternmost part of the seismically active European Cenozoic Rift System, which evolved as a consequence of passive rifting due to compressional stresses during the Alpine and Pyrenean collision (Ziegler, 1992; Plomerová et al., 2016).

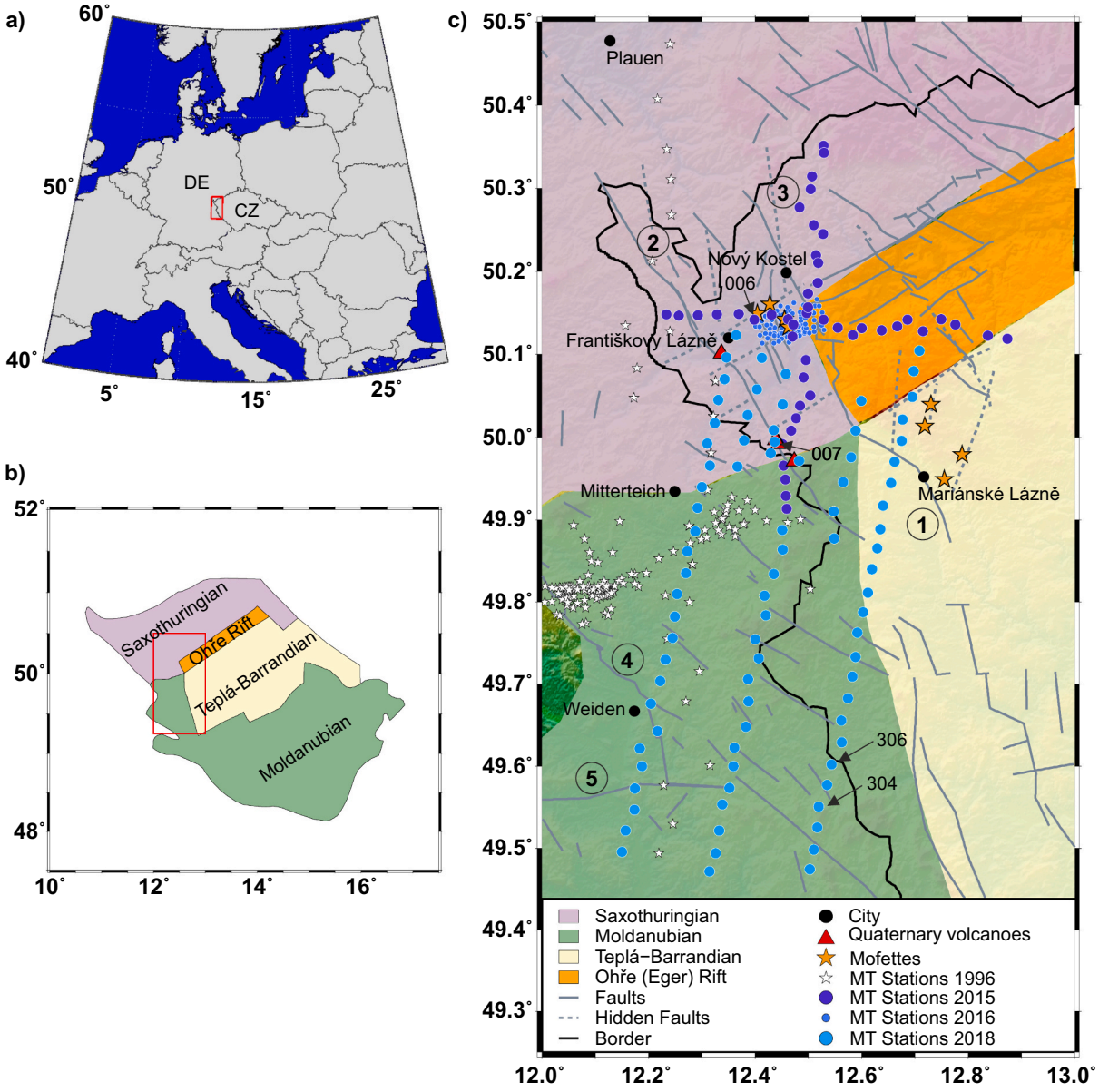

Fig. 1. a) Location map of the study area (red box). The measurements were conducted in Germany (DE) and the Czech Republic (CZ). b) Sketch indicating the three major tectonic units of the western part of the Bohemian Massif. c) Simplified map of the study area showing the MT stations measured in autumn 2018 (cyan circles) as well as MT stations of previous field experiments in this region. The local reference site 304 as well as some other stations are highlighted. Grey solid lines indicate main fault systems with known surface trace as e.g. the Ohře (Eger) Rift, the Mariánské Lázně fault zone (1) and the Aš-Tachov fault (2), while grey dashed lines indicate deep (hidden) faults without surface expression as e.g. the Počatky-Plesná fault zone (3). The two faults Franconian (4) and Luhe (5) line are located in the west of the study area. Mofettes are indicated by orange asterisks and known Quaternary volcanoes and maars are represented by red triangles. (For interpretation of the references to colour in this figure legend, the reader is referred to the web version of this article.)

The 700 *km* long and 40 *km* wide RLRZ is a network of many local faults striking in N-S, NW-SE directions and sometimes also E-W direction (Bankwitz et al., 2003; Fischer et al., 2014; Nickschick et al., 2015). The most important tectonic zones of the RLRZ in the Cheb Basin are the NNW-SSE striking approximately 100 *km* long Mariánské Lázně fault zone (MLFZ) and the Počatky-Plesná fault zone (PPZ) (Bräuer et al., 2014; Fischer et al., 2014). Parallel to the MLFZ runs the Aš-Tachov fault (Fig. 1c); both belong to the younger faults in this region. The ENE-WSW striking main faults of the Ohře Rift form a distinctive Y-shaped structure up to a depth of 15 *km* (Weinlich et al., 1998, 2013; Weinlich, 2014). Furthermore, there exist several NNE-SSW striking deep faults as well as nearly N-S trending faults such as the PPZ (Weinlich et al., 2013; Weinlich, 2014, and references therein). The Cheb–Domažlice Graben is located in the eastern part of the RLRZ and is bounded by the MLFZ to the east and the Aš-Tachov fault in the west (Fischer et al., 2014; Weinlich, 2014). The Cheb–Domažlice Graben intersects the Ohře Rift and Ohře Graben forming the Cheb Basin (Weinlich, 2014; Nickschick et al., 2019). The Cheb Basin, a small intra-cratonic basin at the northwest corner of the Bohemian Massif, developed during the Upper Tertiary and represents the western termination of the Ohře Graben (Bankwitz et al., 2003). The Cheb Basin is filled with up to 300 *m* thick sediments of Tertiary and Quaternary age (Bräuer et al., 2003; Fischer et al., 2014). It is the youngest geological feature in northwest Bohemia (Mousavi et al., 2015).

The western part of the Bohemian Massif belongs to one of the geodynamically most active regions within central Europe and the European Cenozoic Rift System (Plomerová et al., 2016). The entire region is characterized by ongoing magmatic processes in the intra-continental

lithospheric mantle (e.g. Geissler et al., 2005; Bräuer et al., 2009; Kämpf et al., 2013), caused by active magmatic underplating (Geissler et al., 2007; Hrubcová et al., 2017). These processes take place in the absence of active volcanism at surface, but are expressed by a series of phenomena, including e.g. massive degassing of mantle derived CO_2 in form of mineral springs as well as dry and wet mofettes in several degassing fields along tectonic fault zones (e.g. Dahm et al., 2013; Kämpf et al., 2013; Weinlich, 2014) and the occurrence of repeated earthquake swarms (e.g. Horálek and Fischer, 2009; Fischer et al., 2014, and references therein). Active tectonics is mainly manifested by Cenozoic volcanism and neotectonic crustal movements. Seismic studies reveal a complex crustal structure with a wide zone of increased reflectivity in the lower crust at the crust-mantle transition. These lower crustal seismic velocity anomalies can be interpreted as shear zones partly filled with fluids and/or small magmatic intrusions or partial melting that is further suggested by mantle xenoliths (Geissler et al., 2005, 2007). Combined seismological, isotopic and mantle xenolith studies provide evidence that magma accumulation takes place at two different depth levels within the lithospheric mantle at $\approx 60\,km$ and $\approx 25-35\,km$ depth (Geissler et al., 2005, 2007; Heuer et al., 2006). An updoming of the Moho to $25-27\,km$ depth beneath the western Ohře Rift as well as an updoming of the lithosphere-asthenosphere boundary to $65-90\,km$ depth (Babuška and Plomerová, 2001; Heuer et al., 2006), which may include increased partial melt, may represent the common source that supplies the different reservoirs at the crust-mantle boundary (e.g. Ziegler, 1992; Geissler et al., 2005; Heuer et al., 2006). Furthermore, based on different long-term behaviour and levels of the $^3He/^4He$ ratio, Bräuer et al. (2008, 2014) suggest that the upper mantle derived fluids could be supplied from several small spatially separated reservoirs at the crust-mantle boundary with accumulated magma derived from the lithosphere-asthenosphere boundary. A similar observation of an upwelling lithosphere-asthenosphere boundary related to Quaternary volcanism can be found in Algeria (Beccaluva et al., 2007). The complex system of deep reaching faults in this region provides the conditions for the ascent of magmatic CO_2 and forms the only viable migration pathways in the crystalline basement (Weinlich, 2014). The deep seated Y-shaped fault structure of the Ohře Rift splits the ascending magmatic gases at a depth of about $15\,km$ and form several separated degassing centres as well as gas-free zones (Weinlich et al., 1998, 2013). The most prominent degassing centres are the Cheb Basin with the spa Františkovy Lázně (FL) and the spas Mariánské Lázně (ML) and Karlovy Vary (KV) with their numerous mineral springs. In addition, hot springs occur in KV (Weinlich et al., 1998, 2013). In the Cheb Basin, the portion of mantle derived helium was the highest at the PPZ, where the subcontinental helium isotope signature indicates fluid transport pathways down to the deep lithospheric mantle (Fischer et al., 2014).

The intersection area of the Ohře Rift and the RLRZ is furthermore characterized by periodically occurring earthquake swarms with seismic magnitudes up to ML 5 (Heuer et al., 2006; Dahm et al., 2013; Fischer et al., 2014), although the Bohemian Massif is located considerably far away from existing plate boundaries and active volcanoes (Mousavi et al., 2015). Intraplate earthquake swarms without active volcanism are unusual and occur mostly in areas of enhanced crustal fluid activity and in regions with Quaternary volcanism, like the French Central Massif, the Eifel region, Long Valley (California) or Colorado (Horálek and Fischer, 2009). The youngest volcanoes in West Bohemia belong to the late-rift period ($16-0.26\,Ma$) volcanism (Ulrych et al., 2011). The Quaternary activity seems to be restricted to the western border of the Cheb Basin along the Aš-Tachov fault (Hrubcová et al., 2017) and is represented by the two scoria cones Železná and Komorní hůrka (Eisen- and Kammerbühl) as well as by several maar structures such as the Mýtina and the Neualbenreuth Maar.

The areas of Moho updoming, CO_2 emanations and earthquake swarm activities overlap each other indicating ongoing processes in the lithosphere (Heuer et al., 2006). Eighty percent of the seismic energy within the last 25 years was released near Nový Kostel (NK) village (see Fig. 1c), which is spatially correlated with the PPZ (Fischer et al., 2014). As there are no gas exhalations directly above the hypocentres in the vicinity of NK, low-permeable rock units seem to cap the active hydraulic system. The permeability barriers keep the permanent fluid flux from rising further and may be responsible for the increase of the fluid pressure that triggers seismicity (Bräuer et al., 2005).

2.2. Existing electrical resistivity studies

Information on the electrical resistivities of the crystalline basement of the Bohemian Massif and the overlaying geological layers are available from several previous geo-electrical investigations such as MT studies and large- and small-scale electrical resistivity tomography (ERT) experiments. The obtained resistivity models reveal high resistivity values of several hundreds to several thousands Ωm for the crystalline basement and lower resistivity values in the Cheb Basin, at mofettes, for the sedimentary infill of the maars and for regions with fluid interaction.

Several MT studies were conducted in the context of the KTB site in the Upper Palatinate located approximately $10\,km$ west of the current study area (see e.g. Červ et al., 1997a, 1997b; Eisel and Haak, 1999). All of them stress the highly complex geological structure of this region and mention a rather 3D character of the corresponding MT data. Furthermore, these studies emphasize a consistent southern orientation of the real induction vectors (in Wiese convention; Wiese, 1962) for longer periods indicating a conductive structure in the north. Consistent with this hypothesis, Eisel and Haak (1999) state that a strong conductor at the northern end of their profile (that correspond more or less to the northern end of the current study area) is necessary to explain these induction vectors. However, due to limited technical possibilities at that time, the data were almost exclusively explained by 1D and 2D models. Thereby, crustal-scale anisotropic blocks were included to mainly fit the induction vectors together with the observed impedances. In addition, a strong focus was set on shallow macro-anisotropy of the electrical conductivity since borehole logs and samples as well as geological results in the immediate vicinity of the KTB in the Zone Erbendorf-Vohenstrauss (Červ et al., 1997a) indicated graphite, pyrite and brines in fractured sequences. Whether and to what extent this is transferable to the current study area remains unclear as only some stations in the south can be associated with the Zone Erbendorf-Vohenstrauss, if at all. Moreover, Červ et al. (1997a) state that the anisotropy generally decreases towards the east.

Another MT experiment was conducted by Di Mauro et al. (1999) northeast of NK. They report that huge blocks with large anisotropy observed in the close vicinity of the KTB site seem to finish abruptly several kilometres southwest of their target area and thus west of the current study area. They, too, confirm the rather 3D character of the MT data in this region. Their 3D forward model, obtained on the basis of 2D inversion models, displays high resistivity values of the crystalline basement with resistivities $>10^4\,\Omega m$ for greater depths and much smaller resistivity values for the sediments of the Cheb Basin ($10\,\Omega m$).

Recent information about the regional distribution of electrical resistivity came from a MT experiment carried out by Muñoz et al. (2018) within the ICDP project. They measured five-component broad-band MT data along two perpendicular profiles crossing the Cheb Basin and a denser grid of stations close to the mofettes Bublák and Hartoušov. So far, only 2D inversion results of the N-S profile using solely impedance data are published. Large parts of the models presented by Muñoz et al. (2018) show high resistivities ($>1000\,\Omega m$) related to the old crystalline basement. Near the surface lower resistivity values are obtained ($<30\,\Omega m$), especially in the Cheb Basin beneath the Bublák and Hartoušov mofette fields. The most prominent feature in their models is a conductive channel in the vicinity of the earthquake swarm region NK that extends from the lower crust ($\approx 25\,km$ depth) to the surface forming a pathway for fluids into the region of the mofettes. Another conductive channel is present in the south of their models. However, with the given

2D station setup, this feature could not be unambiguously explained. Furthermore, the depth and steepness of this second conductive channel could not be resolved robustly.

A first 3D model of the two regional profiles measured by Muñoz et al. (2018) has just recently been obtained in the framework of a master's thesis (Mair, 2020). Mair (2020) presented results of a joint 3D inversion of impedance and vertical transfer functions. The final 3D model is dominated by high resistivities up to 62,000 Ωm. In contrast, much lower resistivities (<1 Ωm) are resolved close to the mofettes. The most prominent structures are two sub-vertical conductors, which merge into one from a depth of 16 km on forming a conductive reservoir from a depth below 20 km with average resistivities of 80 Ωm and resistivities of 10 Ωm in its central part. One of the two sub-vertical conductors forms a potential pathway for fluids to the mofettes fields and splits into several smaller branches close to the surface. The hypocentres of the earthquakes are located in the resistive host rock surrounding this conductor contrary to the 2D results of Muñoz et al. (2018). The second sub-vertical conductor is located more in the northern part northwest of the earthquake swarm region.

Several other electrical resistivity studies have been conducted in the area of interest such as ERT and Radio-MT experiments. All these methods have in common that they focus on small-scale areas as they have a much smaller penetration depth as the traditional MT method. Several field experiments were conducted using these methods for a characterization of the local electrical resistivity structure of the mofettes (Flechsig et al., 2008; Nickschick et al., 2015, 2019; Rulff et al., 2021), maars (Mrlina et al., 2009; Flechsig et al., 2015; Rohrmüller et al., 2018; Hošek et al., 2019) or the surrounding of the KTB borehole (Storz et al., 2000). The obtained resistivities and their models are only marginally relevant for the current study as they only image the near surface reaching down to a depth of several tens to hundreds of metres. However, they underline that the investigation area is characterized by highly resistive rocks (> several hundreds to thousands Ωm) and that increased conductivity is often connected with the sedimentary infill of the Cheb Basin or the maars. Furthermore, they stress that decreased resistivities are observed for regions with known fluid interaction at e.g. wet mofettes. One of the deepest penetration depth with up to 4 km was reached by a large-scale ERT experiment conducted by Storz et al. (2000) in the close vicinity of the KTB. They resolve resistivity values >1,000 Ωm reaching as far as 10 km east of the KTB. In contrast, Flechsig et al. (2008), Rulff et al. (2021), Nickschick et al. (2019) found clear correlation of an increased conductivity in areas characterized by an ascent and mixture of magmatic fluids such as CO_2 with water.

3. Magnetotelluric data acquisition and processing

The MT method is a passive EM technique to image the electrical resistivity distribution of the subsurface by recording natural variations of the electric and magnetic fields at the Earth's surface. The electrical resistivity is a physical parameter that is particularly sensitive to the presence of high-conductive phases such as aqueous fluids, partial melts, mineralisations or metallic compounds. At each site, two orthogonal, horizontal components of the electric field and three orthogonal components of the magnetic field are measured. In the frequency domain, the different field components are linked by linear relationships which can be described through transfer functions. The period dependent transfer functions are obtained by MT time-series data processing and are subsequently used to model the subsurface electrical resistivity structure. The horizontal electric and magnetic field components are linked by the complex impedance tensor Z that is often visualized as magnitude in terms of apparent resistivity and phase. The vertical magnetic transfer function (VTF) linearly relates the vertical magnetic field component with the two horizontal magnetic field components and is often graphically represented by induction vectors.

Magnetotelluric data of the current study were collected in autumn 2018 at 83 stations along two 75 km and one 50 km long NNE-SSW running profiles as well as some additional stations across the regions of the maars, the Aš-Tachov fault and the suture zones between the different Variscan tectonic units (Fig. 1). The data are published by Weckmann and Platz (2020).

The study area is located south from previous MT measurements within the PIER-ICDP project conducted in 2015 and 2016 by Muñoz et al. (2018). The final results of Muñoz et al. (2018) indicate a conductive channel in the south whose origin could not be unambiguous resolved by the authors due to the given station setup. The station layout of the recently conducted data was designed to overcome this problem by allowing for 2D as well as for 3D inversions. A site spacing of approximately 3 km was chosen along the profiles due to the focus on regional structures, but it still allows the resolution of shallow features. At all stations five-component broad-band MT data were measured in the period range of $10^{-4} - 10^{3} s$ using S.P.A.M. Mk IV magnetotelluric systems, Metronix induction coils and non-polarisable Ag/AgCl electrodes from the Geophysical Instrument Pool Potsdam (GIPP). The recording time at each station was approximately three days, except for station 304 in southeast Bavaria which was used as a local reference station due to its high data quality. The data were processed using the Emerald software suite (Ritter et al., 1998; Weckmann et al., 2005; Krings, 2007). Some regions within the study area are heavily populated and therefore man-made EM noise deteriorates a significant fraction of the recorded time-series severely affecting the MT data quality. To overcome the problem of EM noise, robust single-site and robust remote reference processing were applied in combination with different notch and delay-line filters as well as advanced data selection criteria (Platz and Weckmann, 2019). In addition to the local reference site 304, we used data from the permanent remote station of GFZ located in Wittstock (Ritter et al., 2015) 325 − 400 km north of the survey area. The most obvious outliers in the impedance data and the vertical magnetic transfer functions were manually removed prior to the inversion. Smooth curves could be obtained for the impedance tensor in the period range of $10^{-4} s$ up to 1000 s for many stations. Furthermore, we were able to obtain smooth and stable vertical transfer functions over a wide period range. In general, the data quality decreases from south to north. Moreover, stations close to larger towns as e.g. Weiden, Cheb, and ML are affected by EM noise, whereas more remote stations show noticeable better data quality. For inversion, the newly acquired data set was supplemented by selected and reprocessed stations from Muñoz et al. (2018) measured in 2015 and 2016 as well as by some stations measured in 1996 in the context of the KTB programme.

Fig. 2 displays apparent resistivity and phase curves as well as induction vector plots of three exemplary sites. The location of these three sites is marked in Fig. 1c. The impedance tensor data are shown in a geographic coordinate system (x $\widehat{=}$ north, y $\widehat{=}$ east). Station 306 is located in the southeastern part of the study area, which is characterized by underlying crystalline basement. The shown transfer functions vary smoothly with period. Both off-diagonal impedance tensor components show relatively high apparent resistivity values over the entire period range and large diagonal components for longer periods ($T > 0.1 s$). The real and imaginary induction vectors are presented in Wiese convention (Wiese, 1962) in the lower panel. The real induction vectors for the shortest periods ($T < 0.01 s$) are small and show values close to zero; longer induction vectors are visible for periods greater $T > 0.1 s$. For the longest periods ($T > 50 s$) the real induction vectors are oriented in S-SE direction. Site 007 is located near the Mýtina Maar and the scoria cone Železná hůrka. Here, we still observe high resistivity values for both off-diagonal components and the real induction vectors for the longest periods point towards S-SE. Site EMERES15_006 was measured during the EMERES project in 2015 and has a much higher noise content than the stations measured in 2018, especially for longer periods. The data of this station were reprocessed using the remote reference technique as well as novel pre-selection criteria leading to acceptable transfer functions (Mair, 2020). The apparent resistivities are at least 1–2 decades lower

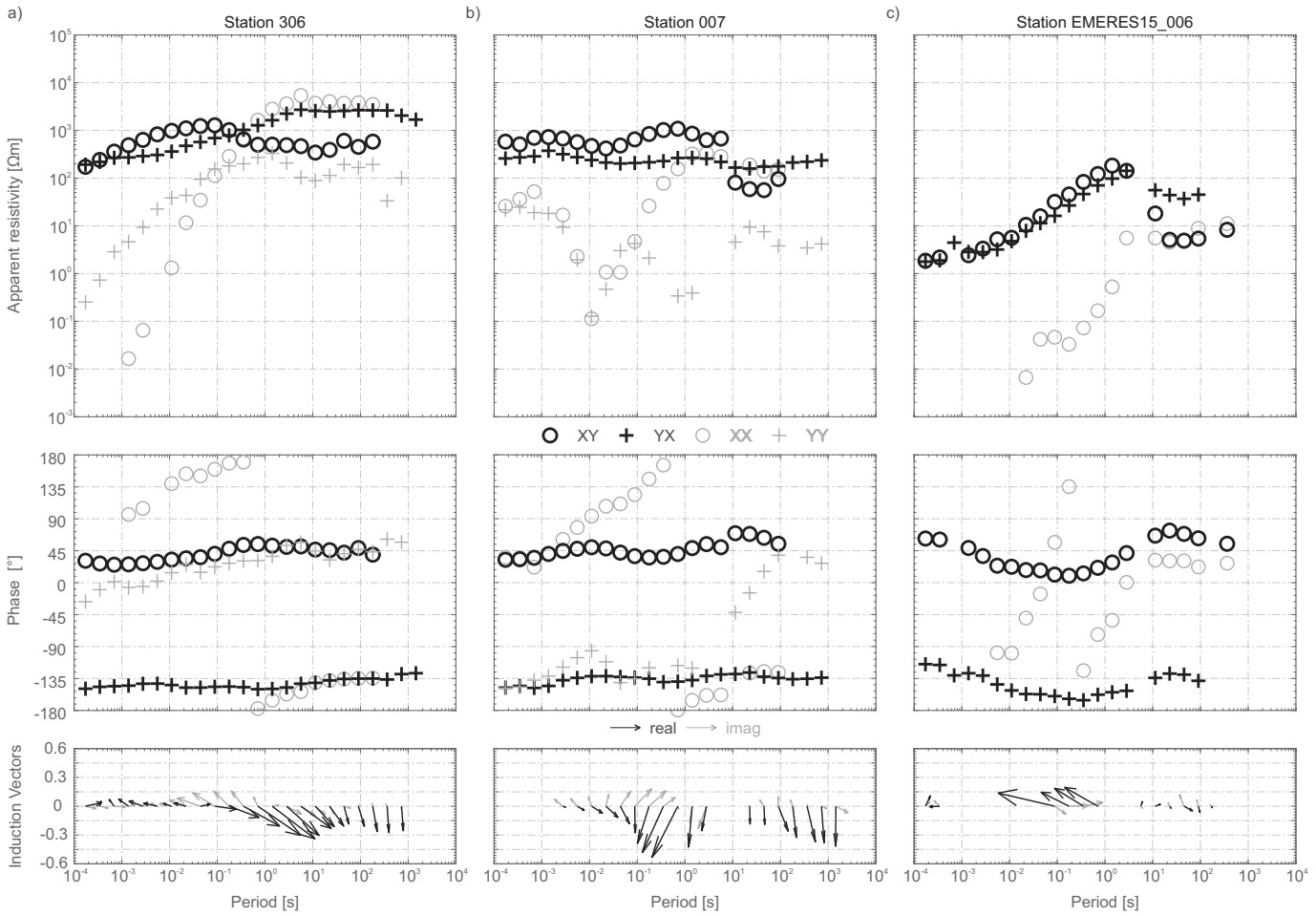

Fig. 2. Off-diagonal and diagonal impedance tensor components shown as apparent resistivity (upper panel) and phase (centre panel) curves as well as induction vectors (lower panel; Wiese convention (1962)) of three exemplary sites (in a geographic coordinate system: x ≙ geographic north, y ≙ geographic east). a) Site 306 is located in Bavaria and is dominated by the crystalline basement. b) Site 007 is located near the Mýtina Maar and scoria cone Železná hůrka and c) site EMERES15_006 is located in the Cheb Basin northwest of the Bublák and Hartoušov mofette fields.

than the apparent resistivity values of the other two stations. This is consistent with the findings of Muñoz et al. (2018), who observed consistently lower apparent resistivity values for stations located within the Cheb Basin. Furthermore, the drop in the apparent resistivity curves for periods longer $T > 10s$ may be explained by a conductive structure at greater depths as this station is located close to several mofette fields. Therefore, we used these data points for the subsequent inversion although it cannot be ruled out that these periods are disturbed by noise. In general, we observe small real induction vectors close to zero for most stations for short periods ($T < 0.01s$) and larger real induction vectors for the longer periods. In the period range between $0.1 - 10s$, the real induction vectors become largest for many stations pointing in several directions dependent of the site location (see Fig. 3a), indicating several spatially limited resistivity structures at depth. For longer periods ($T > 50s$) almost all real induction vectors are orientated in S-SE direction (see Fig. 3b) indicating a conductor in the north.

For the sites along the three longer profiles, the dimensionality of the MT data was determined using the ellipticity method after Becken and Burkhardt (2004, Fig. 4). Thereby, we analysed the dimensionality separately for different period ranges. In general, we observe a large variety of strike angles for the shortest periods for which these values are influenced by shallow structures and do not exhibit common induction spheres with their neighbouring sites. More consistent strike angles as shown by rose diagrams (circular histograms; Fig. 4) are obtained by using both, broader period ranges and longer periods.

The rose diagram for the westernmost profile (hereafter called profile 1; Fig. 4a) clearly shows a clustering of the strike directions of the single-site, multi-frequency strike around $N70^{\circ}E$ (or $N20^{\circ}W$), which corresponds well to the best fit of the multi-site, multi-frequency approach with a strike angle of $N68.9^{\circ}E$ (or $N21.1^{\circ}W$). To solve the inherent 90° ambiguity, we took the direction of the corresponding real induction vectors into account. They are mostly orientated in southeast direction indicating a strike angle of $N68.9^{\circ}E$ for profile 1. In a similar manner, a strike angle of $N74.5^{\circ}E$ for the central profile containing in addition the N-S profile acquired in 2015 (hereafter called profile 2) and a strike angle of $N59.5^{\circ}E$ for the easternmost profile (hereafter called profile 3) were observed. As all obtained geo-electrical strikes point in NE-SW direction, we conclude that the strike direction in the corresponding period ranges are rather dominated by the ENE-WSW trending Ohře Rift than by the different NNW-SSE striking faults. This analysis suggests that the data can be explained by 2D structures in the subsurface. However, given the complex geology of the study area with prominent fault and graben systems running perpendicular to each other (e.g. the Ohře Rift and the PPZ or MLFZ), the presence of the sedimentary Cheb Basin in the north and the different mofette fields and Quaternary volcanoes structures, it is expected that the dimensionality analysis will exhibit 3D characteristics. In addition to the dimensionality analysis after Becken and Burkhardt (2004), we evaluated the phase tensors (see Fig. 3c-f; Caldwell et al., 2004). The distribution of all calculated phase tensor beta values for the entire masked data set in

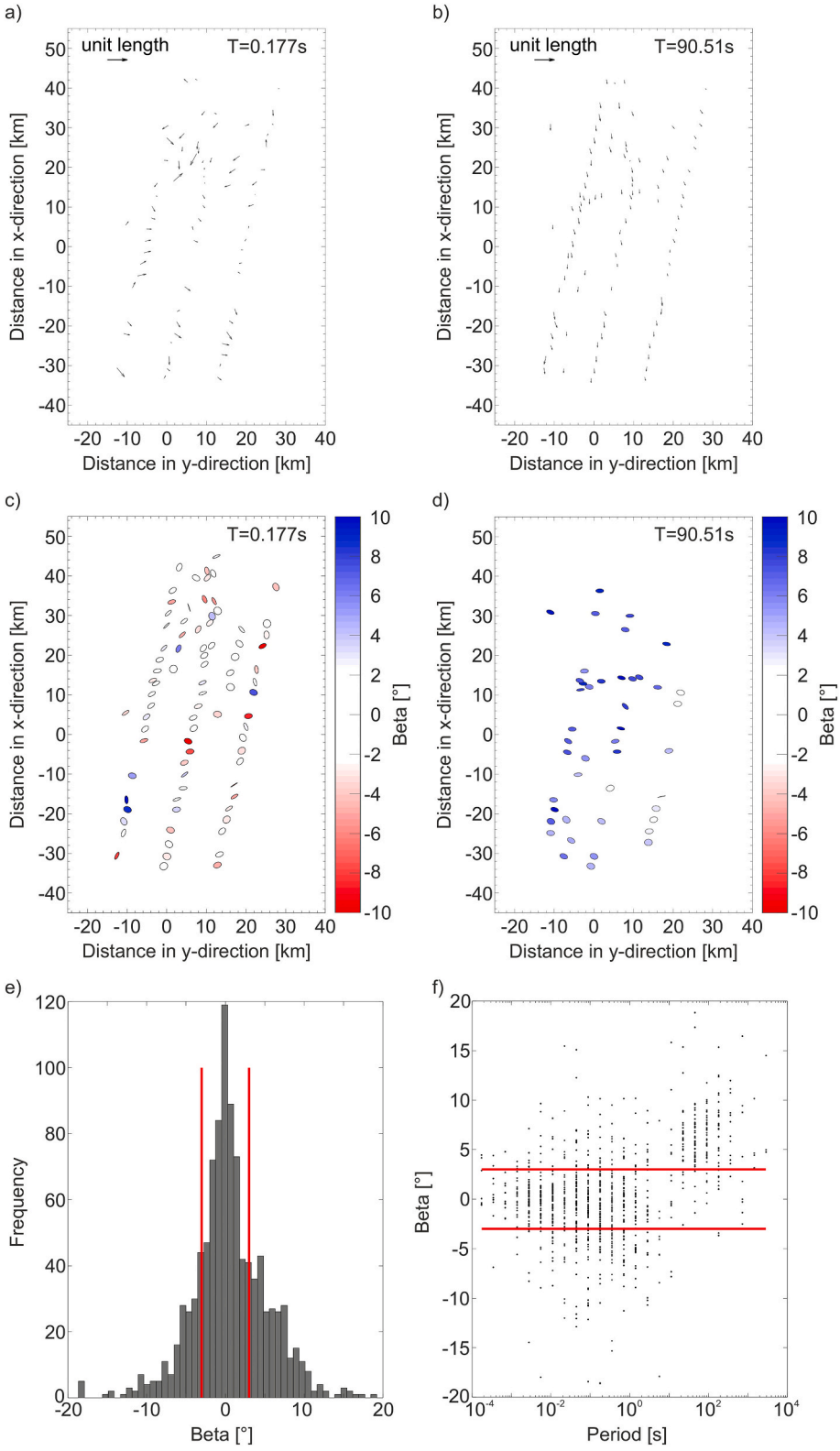

Fig. 3. Maps of the study area showing real induction vectors (in Wiese convention (1962)) for a) $T = 0.177s$ and b) $T = 90.51s$ as well as phase tensors ellipses for c) $T = 0.177s$ and d) $T = 90.51s$. e) Distribution of the phase tensor beta values for the entire data set used for the inversion. 55% of all points have absolute values below 3° (indicated by the red lines) and 1.6% of the data have an absolute value greater than 20°. f) Phase tensor beta values of the data set are shown over period. For periods $T < 1.4s$, the majority of beta values have an absolute value below 3° (indicated by red lines). For longer periods, the majority of the data points have a beta value above 3° indicating a stronger influence of 3D structures. (For interpretation of the references to colour in this figure legend, the reader is referred to the web version of this article.)

Fig. 3e reveals that 55% of the data points have an absolute value below 3°, which is often referred to as a critical value for a reasonable 2D analysis. However, a more differentiated approach shows a correlation between the absolute beta value and the period for this data set (Fig. 3f). For short periods ($T < 1.4s$), the majority of all absolute beta values lies below 3°; however, for longer periods most of the beta values are greater than 3° indicating a stronger influence of 3D structures. This is further demonstrated by means of two maps displaying the phase tensors colour-coded with the corresponding beta values for two different periods (Fig. 3c and d). Moreover, even for short periods, localized areas exist in e.g. the south or in the north close to the mofettes, where higher phase tensor beta values are observed probably due to a more complex subsurface structure. A 2D analysis can address the expected complex 3D geo-electrical structure of the subsurface only within certain limitations,

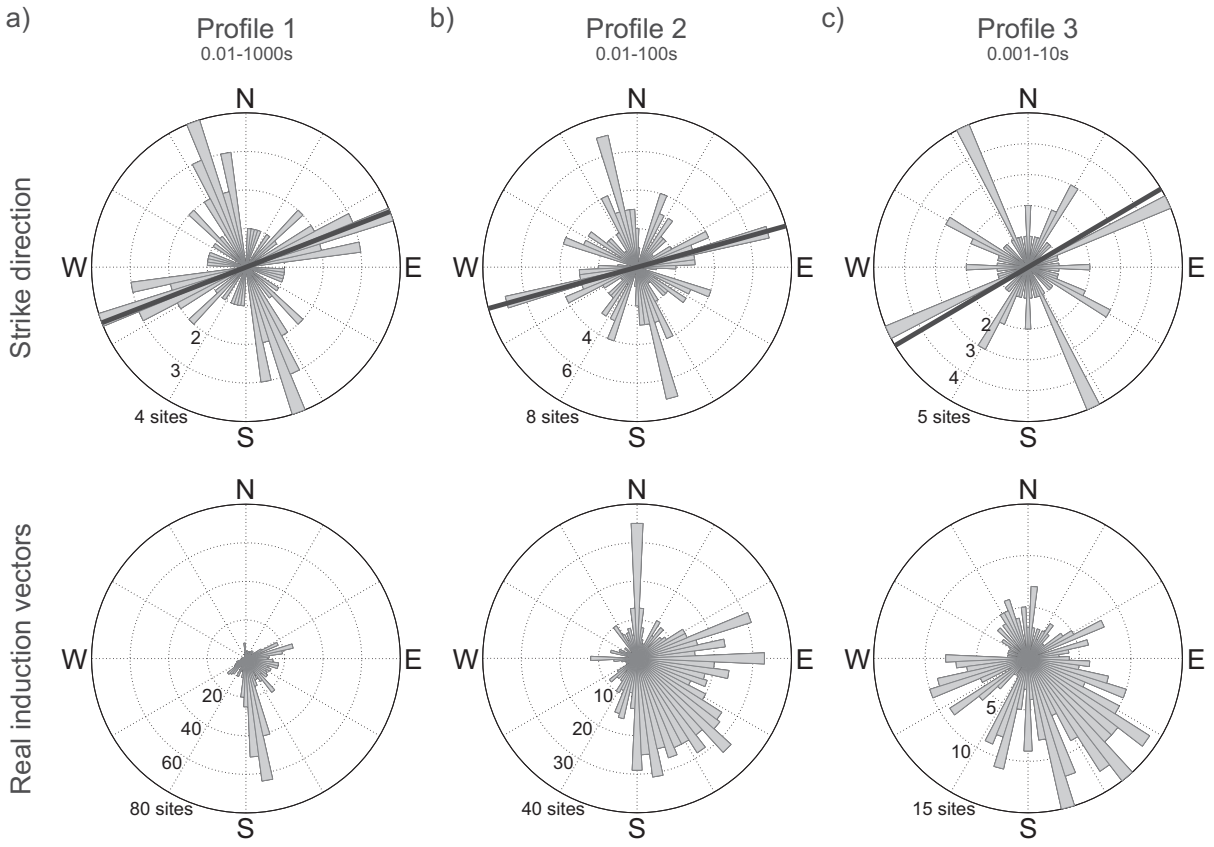

Fig. 4. Rose diagrams of single-site, multi-frequency strike distribution after Becken and Burkhardt (2004, upper panel). The solid black lines represent the best fit for the multi-site, multi-frequency approach, whereby the 90° ambiguity was resolved by considering the preferred direction of the corresponding real induction vectors (lower panel). a) For the westernmost profile (profile 1) a strike angle of $N68.9^{\circ}E$ is obtained for the period range of $0.01 - 1{,}000s$. b) Profile 2 consists of the newly measured data along the central profile and the N-S profile measured in 2015 by Muñoz et al. (2018). For a better comparison with their previous results the period range of $0.01 - 100s$ was evaluated, although we observe only minor changes for adjacent period ranges. A strike angle of $N74.5^{\circ}E$ was retrieved. c) The easternmost profile (profile 3) has a strike angle of $N59.5^{\circ}E$ for the period range of $0.001 - 10s$. For all three profiles the induction vectors are pointing in southeast direction indicating that the strike direction is dominated by the ENE-WSW trending Ohře Rift rather than by the different NNW-SSE striking faults. (For interpretation of the references to colour in this figure legend, the reader is referred to the web version of this article.)

especially as many relevant features will be located off-profile. Therefore, in this paper we will focus on a full-tensor 3D inversion of the entire data set described above.

4. 3D resistivity inversion model

For 3D modelling and inversion we used the parallelized Modular Electromagnetic Inversion system ModEM (Meqbel, 2009; Egbert and Kelbert, 2012; Kelbert et al., 2014). To reduce the computational cost, only every second period of the entire data set were used resulting in 25 periods between $0.000173 - 2896s$. The preferred 3D model presented in this study is obtained through inverting all components of the impedance tensor and the vertical transfer functions for 128 and 105 stations of the entire data set, respectively. The complete data set comprises all 84 stations of the recent field campaigns in 2018, plus 17 reprocessed stations measured in 2015, 7 reprocessed stations from 2016 and 20 stations of the entire KTB data set from 1996. However, most of the stations north of the mofettes measured in 2015 were excluded in order to have a more consistent and even station coverage and due to their poor data quality in comparison to the other data. This also allows a more focused and centred model.

4.1. Model setup and inversion strategy

We conducted more than 200 inversion runs to evaluate different inversion settings and parameters. Important parameters that were tested are e.g. the grid setup, the starting model, the smoothing parameters and the data errors. As a presentation of these tests is beyond the scope of this paper, we will only briefly summarize this point and specify the used parameters for our preferred model.

An initial step in the setup of a 3D model is the specification of an inversion coordinate system and an appropriate model grid. We used a coordinate system with x- and y-axis pointing towards geographic north and east, and the z-axis pointing downwards. The extensions of the grid were chosen much larger than the area of interest amounting to several skin depths in order to obtain accurate forward solutions. We counted on a fine enough parameterization of the model to allow for any near-surface effects, including topographic variations, which were not directly accounted for by the model. We varied the horizontal cell sizes from 750 to $2{,}500m$ trying equal as well as different lengths of the edges for both horizontal directions. Furthermore, we tested the dimension in the vertical direction by varying (i) the number of cells in the z-direction, (ii) the increasing factor (between $1.1 - 1.3$) downwards and (iii) the thickness of the first cell ($5 - 20m$). This first cell also determines the thickness of the first, near-ground air layer that also increases logarithmically upwards. Our finally selected grid consists in total of $112 \times 90 \times 42$ cells covering a modelling area of roughly $9{,}200km$ (N-S or x direction) by $9{,}200km$ (E-W or y direction). The inner grid consists of 62×40 cells with a uniform horizontal dimension of $1.5km$. The padding cells have an increasing factor of 1.3. In the vertical direction, 42 layers

are logarithmically increasing by a factor of 1.3 from 20 m for the first layer down to a total depth of 4,000 km. This depth should be sufficient and represents several skin depths, e.g. more than eight assuming an average resistivity of 1,000 Ωm and a period of 1,000 s.

In the next step, we tested different starting models between 25 – 500 Ωm in order to find a compromise between a low starting misfit (obtained for very low resistivities e.g. 25 Ωm due to the influence of the stations close to the mofettes) and the computed average resistivities for each period (reaching from 250 – 2,000 Ωm). A background resistivity of 300 Ωm was selected as this value resulted in the best inversion result resolving many relevant structures and revealing the best data fit. As mentioned above, the vertical transfer functions seem to require a conductive structure in the north outside of the measurement area. Previous works therefore included crustal-scale anisotropic structures in their 2D models (Eisel and Haak, 1999). After several synthetic tests we found that two remote, but very conductive sedimentary basins need to be included into the starting model: (i) the North German Basin and (ii) the Thuringian Basin (see Fig. 5a). Both structures were finally implemented with 3 Ωm as an integrated resistivity and following the general shape of these basins with an average depth of 4 km and 2 km, respectively.

Furthermore, after testing we only allowed modifications of the resistivity structure made by the inversion in restricted areas. Best results were obtained by fixing the outermost padding cells allowing the inversion to change only an inner part of roughly 950 $km \times 950\,km$. The smoothing values α_x, α_y and α_z were varied between 0.1 – 0.3. Best data fit was achieved by using a smoothing value of $\alpha = 0.1$ for each direction.

In a next step, we tested several error settings and values for the different transfer functions. We varied the error values between 3 – 5% for the vertical transfer functions, between 5 – 10% for the off-diagonal and between 10 – 100% for the main-diagonal impedance tensor components trying constant error values, fixed error values as well as error floors and different types of error calculation (e.g. percentage of $|Z_{ij}|$, $\sqrt{|Z_{ij}{}^{*}Z_{ji}|}$ or $\sqrt{|Z_{ii}{}^{*}Z_{ij}|}$). Finally, we assigned a constant value of 0.05 for the vertical transfer functions and fixed error values to 5% of $|Z_{ij}|$ for the off-diagonal and 20% of $\sqrt{|Z_{ii}{}^{*}Z_{ij}|}$ for the main-diagonal impedance tensor components. Moreover, we tested the sensitivity of the inversion results to sub-sets of data (e.g. only impedance or vertical transfer functions) as well as to different inversion strategies (e.g. joint inversion of impedance and vertical transfer functions and several cascaded inversions using the inversion result of one data type as a starting model for the other data sub-set or the combination of both data types).

4.2. Preferred model

Our preferred model was finally obtained in two steps using a cascaded inversion scheme. First, we inverted only the vertical transfer functions using the 300 Ωm background model including the two sedimentary basins as starting and prior model. The model fits the vertical transfer functions to a normalized root mean square (RMS) of 1.02 (starting from 2.73) after 9 iterations. In the second step, we used the inversion result of the first step as starting model for a joint inversion of impedance and vertical transfer functions. As prior model we used the starting model of the first step. The model fits the full data set to a normalized RMS of 1.8 (starting from 11.16) after 104 iterations. Fig. 6 provides insights into the data fit for the different sub-sets, the data fit over period and compares measured and predicted data for three exemplary stations.

The misfit distribution (Fig. 6a) is rather homogeneously distributed, increasing only slightly from south to north probably due to the different data quality. In general, the best data fit is obtained for the off-diagonal impedance tensor components and for longer periods ($T > 30\,s$) of the vertical transfer functions. We present the preferred model in a series of map views (Fig. 7), cut out models and pseudo-sections (Figs. 8-9) as well as isosurfaces (Figs. 9b and 10) in order to give a spatial impression and to highlight the most important structures.

The overall resistivity of the largest part of the model is very high (R1, resistivities up to 57,000 Ωm) as it can be expected for the old crystalline basement that dominates large parts of the study area (see e.g. Figs. 7c-f and 8). A significant difference for the three Variscan tectonic units cannot be observed. However, slightly increased resistivity values are resolved in the southern part of the study area in the Moldanubian unit (see e.g. Fig. 7c).

For the topmost layer we observe lower resistivities than the 300 Ωm background resistivity for almost the entire study area (Fig. 7a) probably due to a sediment cover or as compensation of near-surface effects such as static shift or topography. Furthermore, a shallow conductive anomaly (C1) occurs in the north between the MLFZ and the Aš-Tachov fault (Figs. 7a-b, 8 and 9) with average resistivities of 20 – 200 Ωm down to a depth of 125 – 250 m. The outline of the conductor C1 (e.g. Figs. 9b and 10) corresponds well with the location of the sedimentary Cheb Basin. Extremely low resistivities down to 0.3 Ωm are resolved close to the spas FL and Sibyllenbad (SB) and nearby the mofettes, although a direct assignment of these anomalies to the individual small-scale structures is not possible due to the comparatively coarse grid. Moreover, the northern part of C1 is characterized by slightly decreased resistivity values (in some parts <20 Ωm) in contrast to the southern part with resistivity values greater than 30 Ωm.

The most prominent structure of the model is a deep reaching conductive channel (C2) with an approximate resistivity of 120 Ωm extending from the surface down to a depth of at least 28 km connecting C1 to a deeper conductive reservoir at a depth of 21 – 28 km (Fig. 10). The conductor C2 has an enhanced conductive part with resistivity values lower than 80 Ωm starting at a depth of approximately 10 km (Figs. 8 and 9c). The lowest resistivities of the conductor C2 of 8 – 10 Ωm

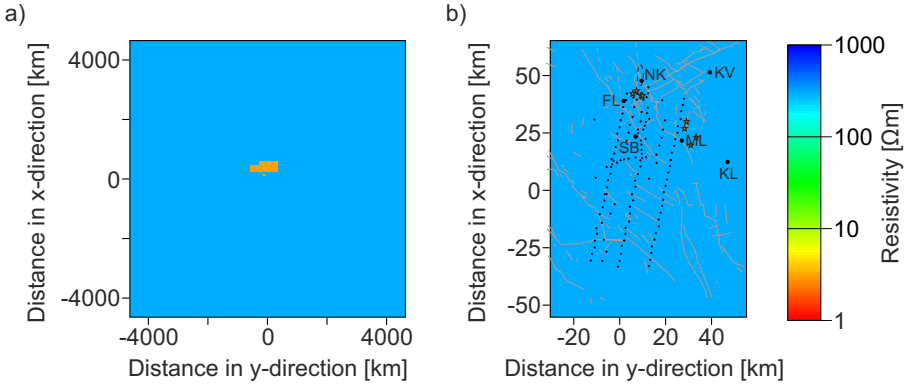

Fig. 5. Map view of the starting model with a background resistivity of 300 Ωm including two sedimentary basins with 3 Ωm and depths of 4 km and 2 km. a) The total extensions of the entire grid covers roughly an area of 9,200 km by 9,200 km. b) The inner uniform grid covers the area of interest. Important faults and hidden faults are marked as solid and dashed lines. Known mofettes are represented by the orange asterisks. The area of the swarm earthquakes around Nový Kostel (NK) is marked by a dashed ellipse. Furthermore, well-known spas are plotted: FL = Františkovy Lázně, ML = Mariánské Lázně, KV = Karlovy Vary, KL = Konstantinovy Lázně and SB = Sibyllenbad.

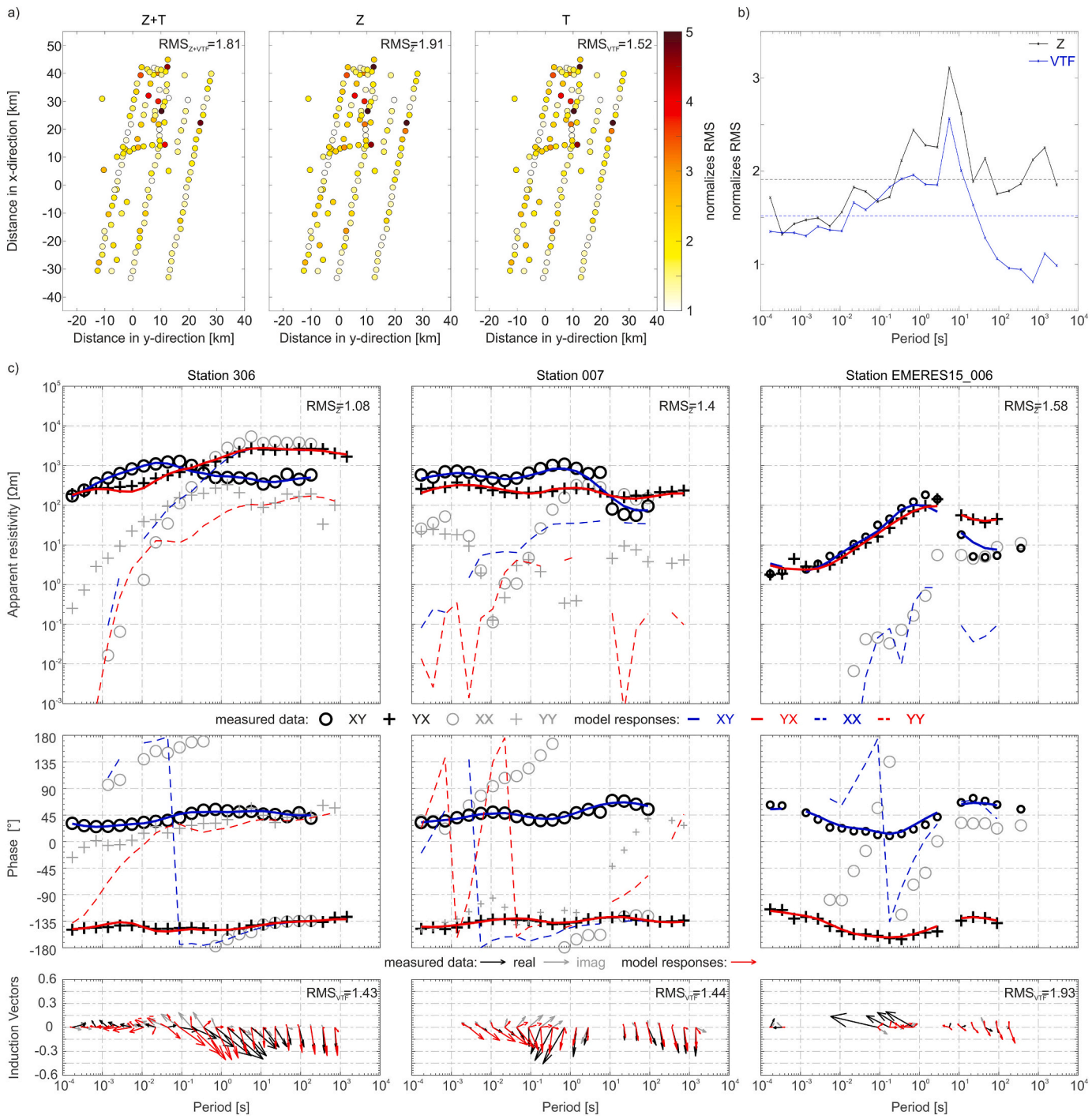

Fig. 6. Data fit of the preferred model. a) Normalized RMS values of the joint inversion and the individual data types Z (impedance) and VTF (vertical transfer function) per station as map view. b) Normalized RMS per period for Z and VTF. The dashed black and blue line represent the overall misfit of 1.91 for Z and 1.52 for VTF. The highest misfit for both data types is observed around the dead band. c) Data fit for the three exemplary stations already introduced in Fig. 2. The individual misfit for Z and VTF for the stations is written on the right upper corner of the corresponding plots. Especially the off-diagonal impedance tensor components and the long periods of the vertical transfer functions are well fitted for all three stations. (For interpretation of the references to colour in this figure legend, the reader is referred to the web version of this article.)

are observed at a depth of $21 - 28 km$ forming a conductive reservoir (Figs. 8, 9a and c).

Closer to the surface, the conductive channel branches into several sub-channels. However, the resolution is poor and not comparable with Muñoz et al. (2018) due to the different sizes of the grids and their cells. The main branch connects the reservoir from the north with the conductor C1 close to the north of profile 1 (Figs. 8 and 9a). Furthermore, the conductor C2 shows a spatial proximity to the NK focal zone (Fig. 7c-f). The hypocentres of the swarm earthquakes cluster around the more conductive part of C2 (Fig. 10).

To the east of the study area, another deep reaching conductive feature can be observed (C3). This conductor is located east of the spa ML with its centre above the spa Konstantinovy Lázně (KL; Fig. 7c-f) approximately $20 km$ away from the easternmost stations. The resolution of the exact geometry and the actual resistivity is limited because large parts of this structure are not covered by the stations. Similar to the

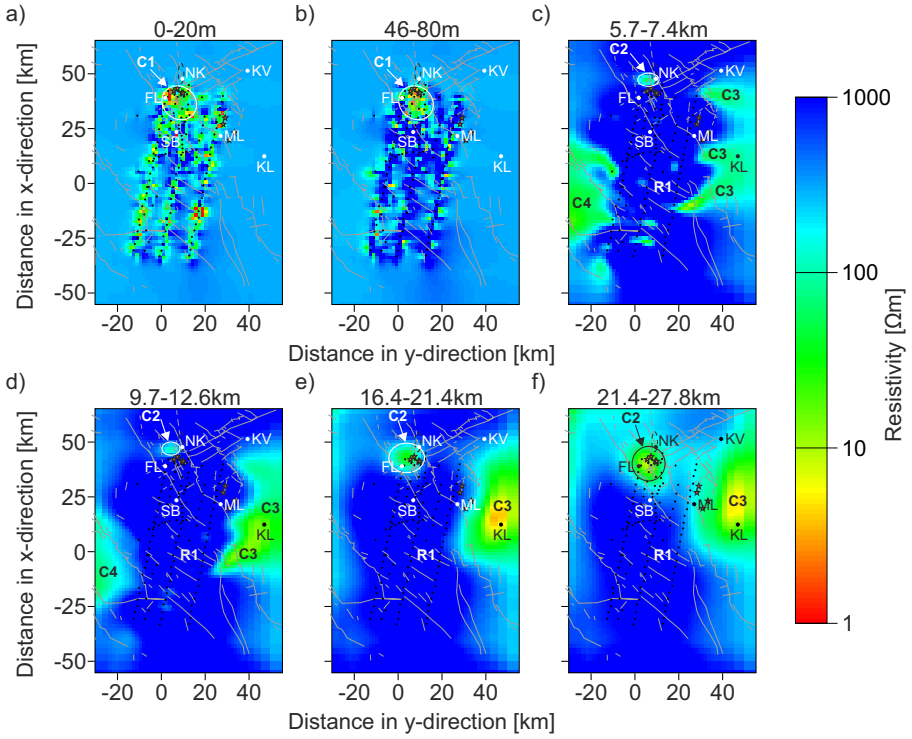

Fig. 7. Resistivity maps for representative layers: MT stations (black dots), mofettes (orange asterisks). a) The first layer is dominated by lower resistivities. b) Lower resistivities of the conductor C1 correlate with the location of the Cheb Basin. c-d) Three deeper conductors (C2-C4) occur below $\approx 5 km$ depth within the resistive structure R1. e-f) The conductors C2 and C3 seem to correspond with the location of known spas such as e.g. FL, ML and KL.

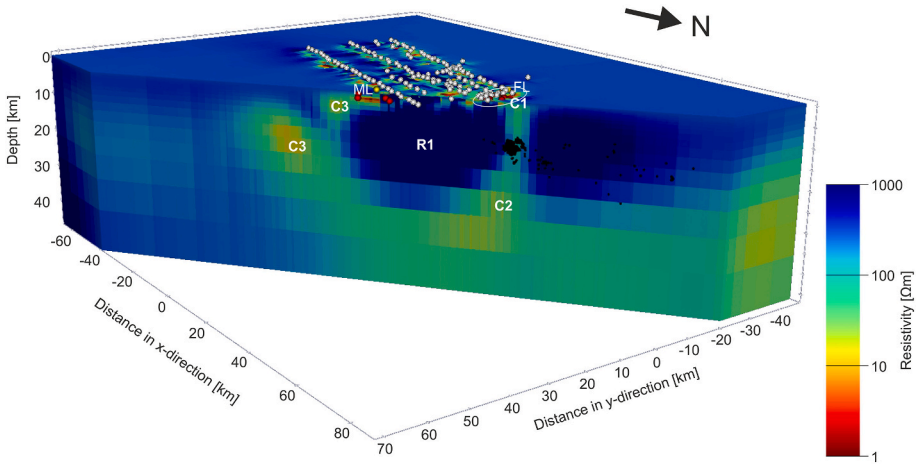

Fig. 8. Southeast-northwest cut through the 3D model along the imaginary connecting line between the two spas FL and ML (yellow dots). The shallow conductive area C1 is marked with a white ellipse. The resistor R1, which probably represents the crystalline basement, is interrupted by the conductors C2 and C3. They might image the pathways for fluid and gas supply close to FL and ML. MT stations (white dots), mofettes (red dots), hypocentres of the earthquakes (black dots). (For interpretation of the references to colour in this figure legend, the reader is referred to the web version of this article.)

conductor C2, C3 has a more conductive part of $3 - 4 \Omega m$ in a depth range of $16 - 21 km$ forming a conductive reservoir (Figs. 8 and 9a). This reservoir is slightly shallower than the reservoir of C2, but has a greater expansion (Figs. 8 and 10). Closer to the surface, the conductor branches into three sub-channels (Figs. 7c and 10). The branch in the south shows low resistivity values between $2 - 5 km$ depth, but does not seem to reach the surface. Between $4 - 5 km$ depth, the middle branch splits again into two branches, one connecting to ML and another one south of ML (Figs. 9 and 10). The northern of these two branches shows lower resistivities close to the surface, which correlate with known degassing centres and springs (Figs. 7a and 8). The lowest resolution has the northern of the three main branches probably due the lack of station coverage. Furthermore, the conductors C2 and C3 seem to be connected at larger depths ($>28 km$); however, resolution studies indicate that, although explaining the data, this connection is not a robust feature and might also be an artefact generated by the inversion and the applied smoothing settings.

In the west, we observe another conductive area (C4) between the two faults Franconian and Luhe line (Fig. 7c-d) at a distance of $1.5 - 6 km$ to the westernmost stations. The outline of this conductor is visualized by an isosurface of $150 \Omega m$ in the Figs. 9b and 10, although the geometry of this conductor can only be resolved within some uncertainties as this structure is located outside the station grid. This area belongs to none of the three Variscan units, but instead is characterized by Permo-Carboniferous and Mesozoic units. Furthermore, the model resolves a conductive structure close to the sedimentary basins in the north outside the study area (not shown), especially beneath the Thuringian Basin. It is also noticeable that conductive structures are absent beneath the volcanic structures or close to the suture zones of the Variscan units or known faults as the Aš-Tachov fault.

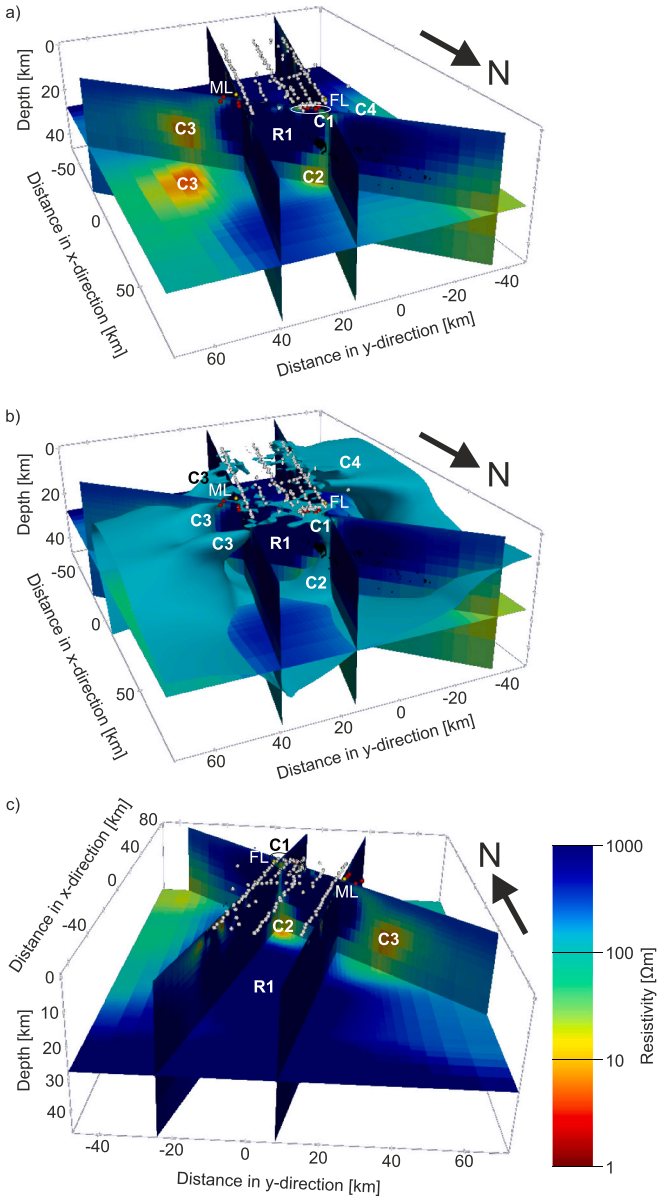

Fig. 9. Pseudo-sections showing the most important structures from different directions. The depth slice corresponds to a depth of 27.6*km*. a) The most prominent conductors C2 and C3 form reservoirs at larger depths and continue in form of conductive channels from the reservoir up to the surface where they seem to correlate with location of mofettes (red dots) close to FL and ML. b) Same pseudo-sections as in a) overlain by a 150Ω*m* isosurface visualizing the different conductive branches of C3 and the shape of the conductor C4 in the southwest. c) Large parts of the study area, especially in the south, are dominated by high resistivities possibly related to the crystalline basement. (For interpretation of the references to colour in this figure legend, the reader is referred to the web version of this article.)

4.3. Sensitivity tests

Several sensitivity tests were performed in order to determine which resistivity structures are required by the data. The depth resolution of the MT data was tested using a "squeeze test". For this test, the resistivity below a certain depth was set to the prior value of 300Ω*m* and the impact of these constraints on the data fit was determined. We did six inversion runs with resistivity fixed below 36, 47, 60, 100, 134 and 175*km*. Significant increases in the normalized starting misfit occur for the three shallowest depths in the squeeze test, although only some stations are affected for the 60*km* depth. This demonstrates that at least in some areas, deeper structures are required by the data. For the shallowest depth of 36*km*, the constrained inversion was no longer able to fit the data as well as for the normal unconstrained inversion. Therefore, we conclude that the MT data can resolve structures up to a depth between 36 and 47*km*, with somewhat greater depths beneath some localized areas.

Next, we tested several shallow small-scale conductive anomalies for example within the conductor C1 or close to ML. For this purpose, we substituted cells with extremely low resistivities (e.g. <3Ω*m*) by average resistivity values of the surrounding cells (e.g. 20Ω*m*) and calculated the forward response of these modified models as well as we started new inversions from these modified models. The forward models show an increased misfit close to stations, where changes were made. Moreover, the inversions tend to recover many of these small-scale conductive anomalies, especially within the conductor C1 and around ML. In summary, we conclude that these shallow small-scale conductive anomalies close to the spas and mofettes in the Cheb Basin and the surrounding of ML are required by the MT data.

Furthermore, we tested the resolution of the two most striking conductors C2 and C3. This is of great importance, especially for C3, as large parts of this conductor are not covered by stations and thus the validity of certain parameters such as its exact geometry is limited. The vertical extend of these conductors were tested by replacing deeper parts (>2.5*km*) of these conductive anomalies by the background resistivity of 300Ω*m*. Again, forward calculations and new inversions were started from the modified models. The forward models show that for the modified models the misfit at the neighbouring stations is considerably increased. Further, the inversions tend to recover the vertical conductor C2 as well as all three branches of conductor C3 and especially the southern branch of C3. In a next step, we substituted only the "reservoirs" of C2 and C3 at a depth of 16.4*km* by the background resistivity. The misfit of the forward calculation of this modified model was increased. An inversion started from this modified model recovers especially the reservoir beneath ML, and to some extent the smaller and more resistive reservoir of C2. Further tests on possible connection of the deepest parts of C2 and C3 reveal that the reservoirs could also be separated without resulting in an increased RMS. This suggests that the inversion and the recorded data have no sensitivity for the deepest parts of C2 and C3, however, this also means that a connection of both conductors at depth is not explicitly excluded.

The resolution of the conductor C4 was tested, as it is hardly covered by stations. Therefore, we substituted the lower resistivity values of C4 by the background resistivity. The misfit of this modified model is significantly increased, especially for the surrounding stations of profile 1 in the southwest. An inversion started from the modified model recovers large parts of the conductor C4, indicating that this conductor is needed by the data. Furthermore, the new inversion tends to recover the reservoirs of C2 and C3 with lower resistivity values, e.g. with down to 5 − 6Ω*m* for the most conductive parts of C2. If we fix the area of C4 to the background resistivity of 300Ω*m*, the inversion misfit increases, especially in the south and the inversion is not able to find an alternative model that explains the data as well as the unconstrained inversion.

Finally, we tested the conductive structures close to the two sedimentary basins in the north outside the study area, which we implemented in our starting model. We excluded the basins from our preferred model and replaced them with the background resistivity. The forward calculation of this modified model has a larger misfit, especially for the vertical transfer functions. The subsequent inversion recovers conductive features in the north in the area of the Thuringian Basin, indicating that the vertical transfer functions require some conductive features in the north outside the study area, e.g. the two basins or some other conductor. Furthermore, the new inversion resolved the two reservoirs of C2 and C3 with lower resistivity values down to <4Ω*m* for C2 and down to <3Ω*m* for C3. The necessary existence of a conductive feature in the north was further supported by another test: We fixed the two

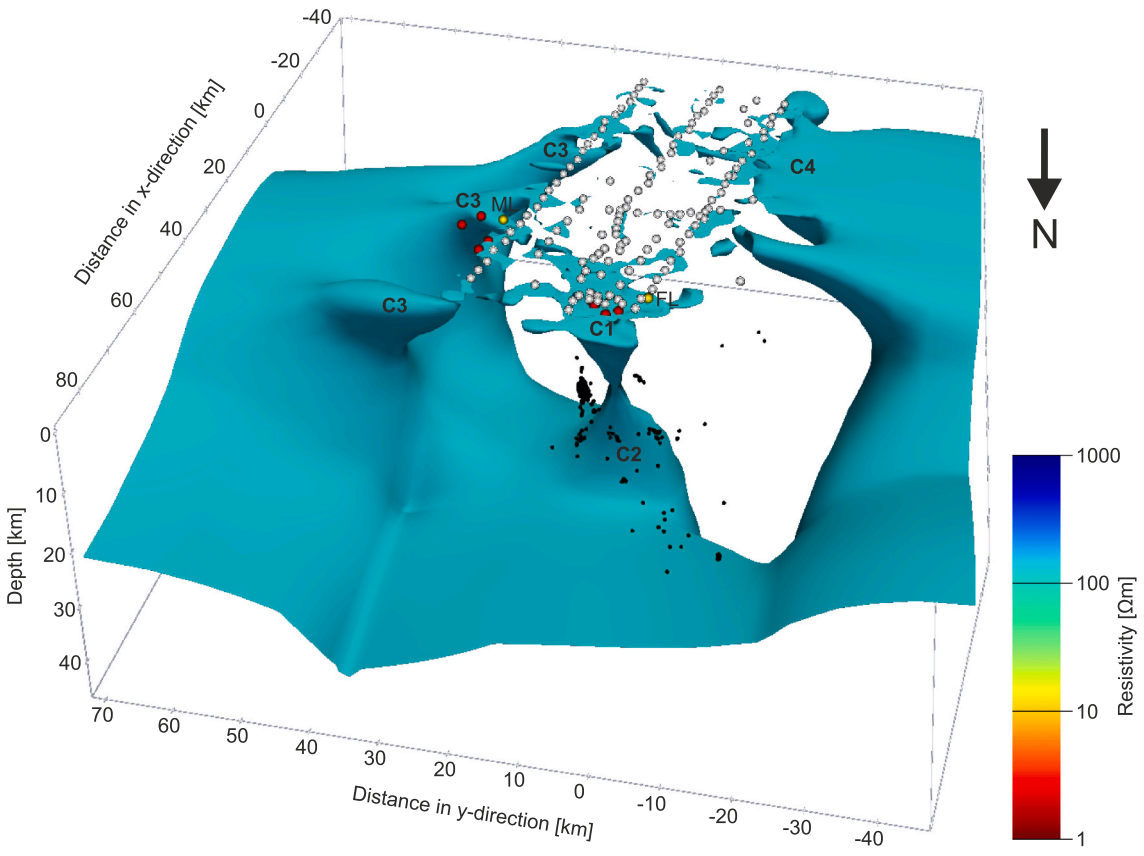

Fig. 10. Isosurface of 150 Ω*m* imaging the shape of the conductors C1-C4. Many of the swarm earthquakes (black dots) are mostly located in the resistive host rock surrounding conductor C2.

basins in the preferred model to the background resistivity of 300 Ω*m* and the subsequent newly started inversion was unable to fit the long periods of the vertical transfer functions.

4.4. Discussion

The largest part of the preferred model is dominated by the extensive resistive body R1. Its upper boundary is located in the upper crust starting at approximately several hundreds of metres and continues down to the maximum resolution depth of 36 – 47 *km*. The high electrical resistivities up to 57,000 Ω*m* can be associated with the crystalline basement and they match well with observed and modelled resistivity values of previous MT studies (e.g. Di Mauro et al., 1999; Muñoz et al., 2018; Mair, 2020, and references therein) as well as resistivity values for crystalline (igneous) rocks of the continental crust from literature (e.g. Haak and Hutton, 1986; Simpson and Bahr, 2005; Chave and Jones, 2012). Although a significant resistivity variation between the three tectonic units is not resolved, a noticeable decrease of resistivity is observed for the units of the Permo-Carboniferous and Mesozoic in the west (C4). From previous measurements in the framework of the KTB investigations it is known that these units show much lower resistivities than the crystalline basement of the Variscan units (see e.g. Eisel and Haak, 1999; Eisel et al., 2001; Storz et al., 2000).

The relatively low resistivities of the first layer for almost the entire study area can be associated with a sedimentary cover and/or is a compensation of near-surface effects as e.g. static shift or topography, which were not explicitly addressed by the model and are therefore not further interpreted. The shallow conductor C1 is spatially correlated with the Cheb Basin and is restricted by the MLFZ in the east and the Aš-Tachov fault in the west. Its estimated depth of 125 – 250 *m* fits well with the known geology, which characterizes the Cheb Basin as a up to 300 *m* thick basin filled with sediments of Tertiary and Quaternary age (Bräuer et al., 2003; Fischer et al., 2014). These unconsolidated sediments are responsible for the observed average low electrical resistivities of 20 – 200 Ω*m*. Further, these resistivity values match well with the observed and modelled values for the Cheb Basin from previous MT studies in the area by Di Mauro et al. (1999) and Muñoz et al. (2018). The shallow small-scale conductive anomalies within C1 with resistivities down to 0.3 Ω*m* spatially correlate with the known spas FL in the western Cheb Basin and SB in the south. Furthermore, the locations of these small-scale conductive anomalies can be associated with the locations of several mofette fields as e.g. the Bublák and Hartoušov mofette fields or the Soos national nature reserve. Sensitivity tests indicate that these small-scale structures are required by the data. Furthermore, Mair (2020) also resolved low resistivities <1 Ω*m* close to the mofettes. However, direct correlations of the small-scale anomalies with the individual degassing centres are beyond the scope of this paper and were not possible due to the grid size required for the regional perspective. However, a localized increase of the electrical conductivity correlated with the ascent of fluids would correspond with the findings of other small-scale electrical resistivities studies conducted in the vicinity of known degassing centres in this region (e.g. Flechsig et al., 2008; Nickschick et al., 2019; Rulff et al., 2021). Moreover, the slightly increased resistivities in the southern part of C1 can be spatially associated with the gas-free zone in the southern Cheb Basin described by Weinlich et al. (1998, 2013).

One of the most striking resistivity features in the model is the deep reaching conductive channel C2. We interpret this conductor as a fluid pathway from the lower crust to the surface similar to Muñoz et al. (2018). This conductor connects a potential fluid/magma reservoir at the crust-mantle boundary with the degassing centres within the shallow conductor C1 (see Fig. 11). However, the split of C2 at shallower depths

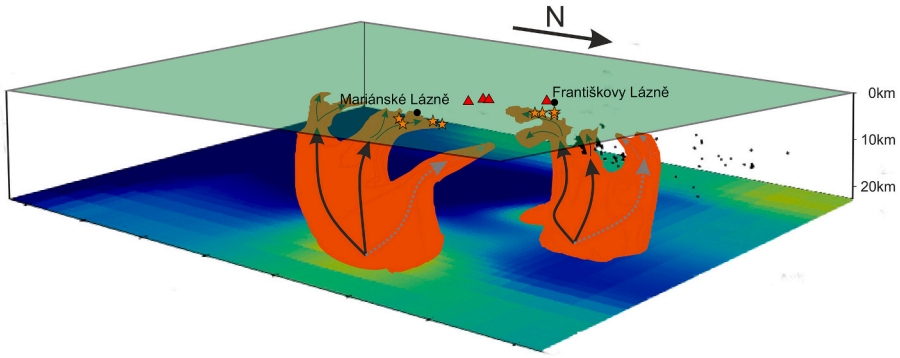

Fig. 11. Sketch illustrating the geodynamic situation in the study area derived from the preferred model and the 3D model of Mair (2020). The different degassing centres (e.g. mofettes, represented by orange asterisks, and the spas FL and ML) may be supplied from different spatially separated fluid/magma reservoirs in the lower crust at the crust-mantle transition zone. The potential pathways for fluids and/or gas branch into several smaller pathways at larger depths as well as close to the surface. Pathways with a low data resolution are marked by dashed grey arrows. The hypocentres of the swarm earthquakes (represented by black dots) scatter around the potential fluid pathways. Both models do not resolve any potential pathways to the volcanic structures (red triangles). (For interpretation of the references to colour in this figure legend, the reader is referred to the web version of this article.)

towards the individual degassing spots is only partly resolved by our model due to the limited grid resolution. In contrast to Muñoz et al. (2018), the conductor C2 is now located more to the west of profile 1, indicating that the northern conductive channel in their 2D model is a projection of the conductor C2 resolved in the 3D model. Similar to the 2D model of Muñoz et al. (2018), the conductor C2 has a more conductive part at larger depths ($>10\,km$) and reaches its lowest resistivity values of $8-10\,\Omega m$ in a depth range of $21-28\,km$. In addition, shape, location, resistivities and the split of this conductor C2 close to the surface match well with those of the conductor resolved by the 3D inversion of the two regional profiles by Mair (2020). Following the explanations of Muñoz et al. (2018, and references therein), the CO_2–H_2O system in the faults change from a single phase system with dissociated ions to a two phase system with gas state CO_2 bubbles at a depth of roughly $9.6\,km$ in the study area. Therefore, the shallower parts of the conductor C2 can be associated with the more resistive two phase system of the ascending fluids, whereas the deeper and more conductive part of C2 is represented by the more conductive single phase system of these fluids. The most conductive part of C2 can be associated with one of the crust-mantle reservoirs postulated by Bräuer et al. (2008). The transition from the single phase system to the two phase system in the Cheb Basin is expected at a depth range of $6-11\,km$ (Weinlich, 2014) and corresponds well with the depth of the hypocentres of the swarm earthquakes. Our 3D inversion model strongly suggest that the earthquakes are located in the resistive surrounding of conductor C2. These findings are confirmed by local scale 3D models of Mair (2020). A real MT experiment across the San Andreas Fault in California revealed a similar result. Becken et al. (2011) reported that brittle rock failure and earthquakes often occur close to the boundary of, or within, regions of high electrical resistivity, but adjacent to zones of low resistivity. They explain these observations at the San Andreas Fault through the migration of fluids from a permeable, mechanically weak source region into a less permeable, mechanically strong zone of high electrical resistivity. Similar observations were reported by e.g. Ogawa et al. (2001, 2014) for the Japanese back arc, Comeau et al. (2015) for a volcano in Bolivia or by Aizawa et al. (2021) for volcanoes in Japan. As the 2D model of Muñoz et al. (2018) is located east of the focal zone, they could only use projected locations of the earthquake hypocentres that likely resulted in their misleading interpretation that the earthquakes would be located within the conductive structure. A seismic study of Mousavi et al. (2015, 2017) reveals an anomalous crustal body located just below and north of the NK focal zone that is characterized by high v_p values and high v_p/v_s ratios. This anomaly spatially correlates with the shape of conductor C2. Mousavi et al. (2015) interpreted this anomaly as a solidified intrusive body which contributes to the triggering of earthquakes by delivering fluids into the focal zone. Furthermore, they assume that this mid-crustal intrusive body could be part of a fluid pathway from the mantle through the earthquake zone up to the mofette fields in the south at the surface. This would support our hypothesis that C2 is a fluid pathway from the lower crust to the surface and the associated degassing centres.

To the east of the study area, another deep reaching and prominent conductive structure (C3) is observed. Similar to C2, we interpret this conductor as a fluid pathway from the lower crust to the surface (see Fig. 11). The exact shape and extension of this conductor can be slightly different as resolved in the 3D model due to the sparse station coverage. However, its existence and its splits into several branches were confirmed by several sensitivity tests. The conductor C3 consists of a large reservoir at depth and several conductive branches that connect this reservoir to the surface. The reservoir is larger and more conductive than the reservoir associated with C2. Furthermore it is located at a slightly shallower depth, supporting the hypothesis of Bräuer et al. (2005, 2008) of small-scale spatially separated magmatic reservoirs. Based on different long-term behaviour and levels of the $^3He/^4He$ ratio, they postulate that the degassing centres in the Cheb Basin and around ML are supplied by different small and isolated reservoirs at the crust-mantle boundary. In general, the depth ranges of the deep reservoirs of the conductors C2 and C3 fit reasonably well with other combined seismological, isotopic and mantle xenoliths studies, which describe a magma accumulation in a depth range of $25-35\,km$ (Geissler et al., 2005; Heuer et al., 2006; Geissler et al., 2007). The southern branch of C3 correlates neither with a known fault, a volcanic structure nor with a degassing centre. This can possibly be explained by the fact that this branch does not reach the surface. The middle branch of C3 forks at a depth of $4-5\,km$. The northern part connects to the degassing centres around ML and shallow small-scale conductive anomalies spatially correlate with known mofettes. The northern branch of C3 has the lowest resolution possibly due to the sparse station coverage in the northern part. This conductor might represent a fluid pathway to the famous spa KV. However, due to the limited resolution in this part this remains speculative.

Finally, it is noticeable that conductive structures are absent beneath the volcanic structures, close to the suture zones of the Variscan units or the Aš-Tachov fault along the stations of profile 2. Therefore, we conclude that the southern conductor observed in the 2D model of Muñoz et al. (2018) is very likely a projection of another conductive off-profile structure. Based on the spatial proximity, the middle branch of conductor C3 would be the most obvious explanation for the conductor observed in the previous 2D model. To examine this hypothesis, we compare the 3D model with newly conducted and the previous 2D inversion results in the next section.

5. Comparison with 2D inversion results

For the 2D inversions of the three long profiles we used the finite element code MARE2DEM (Key and Ovall, 2011; Key, 2016).

MARE2DEM uses a goal-oriented adaptive finite element method for the forward solutions that automatically generates and refines unstructured triangular element grids. We ran between 70 − 200 inversions for each profile testing several inversion settings and parameters e.g. different grids, starting models, data errors or different input data (apparent resistivity and phases, logarithm of apparent resistivity and phase, vertical transfer functions and combinations of them). A presentation of these tests is beyond the scope of this paper; and moreover, they often resulted in similar inversion models demonstrating the robustness of the obtained models. For better comparison with the 2D result of Muñoz et al. (2018) (hereafter called EMERES15), we show only inversion results using rotated apparent resistivity and phase curves. Moreover, all 3D and 2D results are shown without smoothing.

A simplified topography was included in all 2D inversion grids and the rotated data were projected onto profiles perpendicular to their respective strike angles. As starting models we used homogeneous half-spaces. For the three profiles, the subsurface was discretized with 26,000 − 33,000 cells. We forced the cell sizes of the finite element grid to mainly grow with depth by defining eight boxes centred around the stations with depths between $100m$ and $200km$ below surface and increasing widths. The edge length within each box was kept constant growing from $100m$ for the shallowest box up to $7km$ for the lowest box. For the EMERES15 profile the subsurface was coarser discretized with roughly 12,000 cells using three boxes up to a depth of $6km$. The trade-off Lagrange multiplier was set to 5 in all inversions and as weight between horizontal and vertical smoothness a factor of 3 was used. For the three profiles of the current field campaign we inverted 51 periods between $10^{-4} - 4{,}096s$, while Muñoz et al. (2018) could use only periods up to $362s$. To reduce the influence of static shift, the apparent resistivities, in particular of the transverse electric (TE) mode, were down-weighted and a higher weight was given to phases by choosing small errors for them. The error for the apparent resistivity of the TE mode was set to 50% (profile 1 and 2) and 100% (profile 3 and EMERES15), meanwhile we used much smaller errors of 10% (profile 1 and 2) and 20% (profile 3 and EMERES15) for the apparent resistivities of the transverse magnetic (TM) mode. Constant errors of 2° (profile 1 and 2) and 3° (profile 3 and EMERES15) were used for the phases of both modes. The data used for the EMERES15 profile were furthermore shifted for some stations by a constant factor for each station and mode to correct for static shift. Other important parameters for the three profiles as well as for the EMERES15 profile are summarized in Table 1.

Before we discuss differences and similarities between 3D and 2D inversion results, we compare the 2D inversion result of profile 2 (Fig. 12b) with the EMERES15 model (Fig. 12e).

Profile 2 uses data from the same stations as EMERES15 plus the data of 17 stations conducted in 2018. However, the data are rotated by different angles and as a result projected to slightly different profiles. Furthermore, the grid used for EMERES15 is noticeable coarser than the grid for profile 2. The conductor C1 in the centre of the EMERES15 profile associated with the Cheb Basin can also be observed for profile 2.

Table 1
Inversion parameters for the three profiles measured in 2018 and the inversion result of Muñoz et al. (2018).

	Profile 1	Profile 2	Profile 3	EMERES15
Number of stations	25	17 / 25	25 / 1	25
Year	2018	2018 / 2015	2018 / 2015	2015
Rotation angle of the data	−111.1°	−105.5°	−120.5°	−125.0°
Background resistivity of starting model	$100\Omega m$	$700\Omega m$	$700\Omega m$	$500\Omega m$
Number of free grid parameter	32,989	28,850	26,135	11,652
Final / Starting RMS	1.7 / 33.63	2.07 / 58.97	1.17 / 11.07	1.9 / 57.48
Iterations	86	109	162	?

Furthermore, two conductive channels C2 and C3 are resolved in both models. Even the split of C2 close to the surface in two branches can be observed in both cases. However, the vertical conductors C2 and C3 are much thinner in profile 2 very likely due to the finer grid. The conductor C3, which could only be resolved poorly for EMERES15 due to the lack of stations, forks into two branches in profile 2. Lower resistivities at larger depths are observed for C2 and C3, similar to EMERES15, although the depth and conductivities itself differ between the two models. In both models, the conductors C2 and C3 are separated by a large resistor R2 and another resistive feature R1 is resolved in the north. Solely the resistivity values of the resistors differ, probably because some of the data used for the EMERES15 profile were corrected for static shift and therefore shifted to lower resistivity values. Nevertheless, despite all the differences, the 2D models show many similarities. All important conductors and resistors interpreted by Muñoz et al. (2018) are resolved in the northern part of profile 2, which coincides with the EMERES15 profile.

For a comparison of the 2D results with the 3D result, we show sections through the preferred 3D model along the real locations of the corresponding stations (Fig. 12a and d) and adjusted the colour scale of the 3D model. The cut through the 3D model along profile 2 shows lower resistivities close to the surface in the northern part associated with the Cheb Basin and consistent with the 2D results. However, many of the other structures visible in the 2D models of profile 2 and EMERES15 as the vertical conductors C2 and C3 are absent in the section from the 3D model, instead a deeper conductor associated with the reservoir beneath the Cheb Basin is discernible. This supports the idea that the 2D results are affected by some 3D and/or off-profile structures. Cruces-Zabala et al. (2020) systematically tested and assessed the influence of off-profile structures on 2D models obtained by MARE2DEM using real and synthetic data from Venezuela. They demonstrate that off-profile conductors can be mapped into 2D models as long as the station data are influenced by these structures. Furthermore, they show that the shape and inclination of conductors crossing the profiles, e.g. conductive faults, can differ from their true location and dip depending on the projection of the stations onto the profile. As we showed in the 3D section above, a vertical conductor in the north exists located west of profile 2. This conductor C2 in the 3D model is very likely projected into the 2D models and corresponds to the conductor C2 of these models. The vertical conductor C3 in the south of the 2D models is also not visible in the 3D model along profile 2 (Fig. 12a). A possible explanation for this conductor C3 in the 2D models, is a projection of another off-profile conductor, e.g. the conductor C3 of the 3D model close to ML, into the 2D model. To verify this hypothesis, we conducted synthetic 2D inversions. A forward calculation of the preferred 3D model using the real station layout was conducted to generate the data for this synthetic inversion. 5% Gaussian noise was added to the synthetic data consistent with the applied error for the 3D model for the off-diagonal impedance tensor components. Then, the synthetic data were rotated and projected in the same manner as the real data for the subsequent 2D inversions. For a better comparison, the same inversion settings, e.g. grid, starting model and error settings, as for the 2D inversions of the real data were used for the synthetic 2D inversions. Differences were made only for the EMERES15 profile as we did not correct the data for static shift. The results of the synthetic inversions for profile 2 and EMERES15 are shown in Fig. 12c and f. Interestingly, they show many similarities to the 2D inversion results of the real data (Fig. 12b and e). The shallow lower resistivities associated with the Cheb Basin are observed for both synthetic models. Furthermore, the conductive channel C2 in the north is visible in profile 2 as well as in the EMERES15 profile, supporting our statement that the conductor C2 from the 3D model located west of profile 2 is projected into the 2D models. Moreover, another conductive channel in the south is visible in both synthetic models. While the channel for the EMERES15 profile differs from its dip and location from C3 of the real data, larger similarities are observed for the real and synthetic inversion along profile 2. For the synthetic inversion of profile

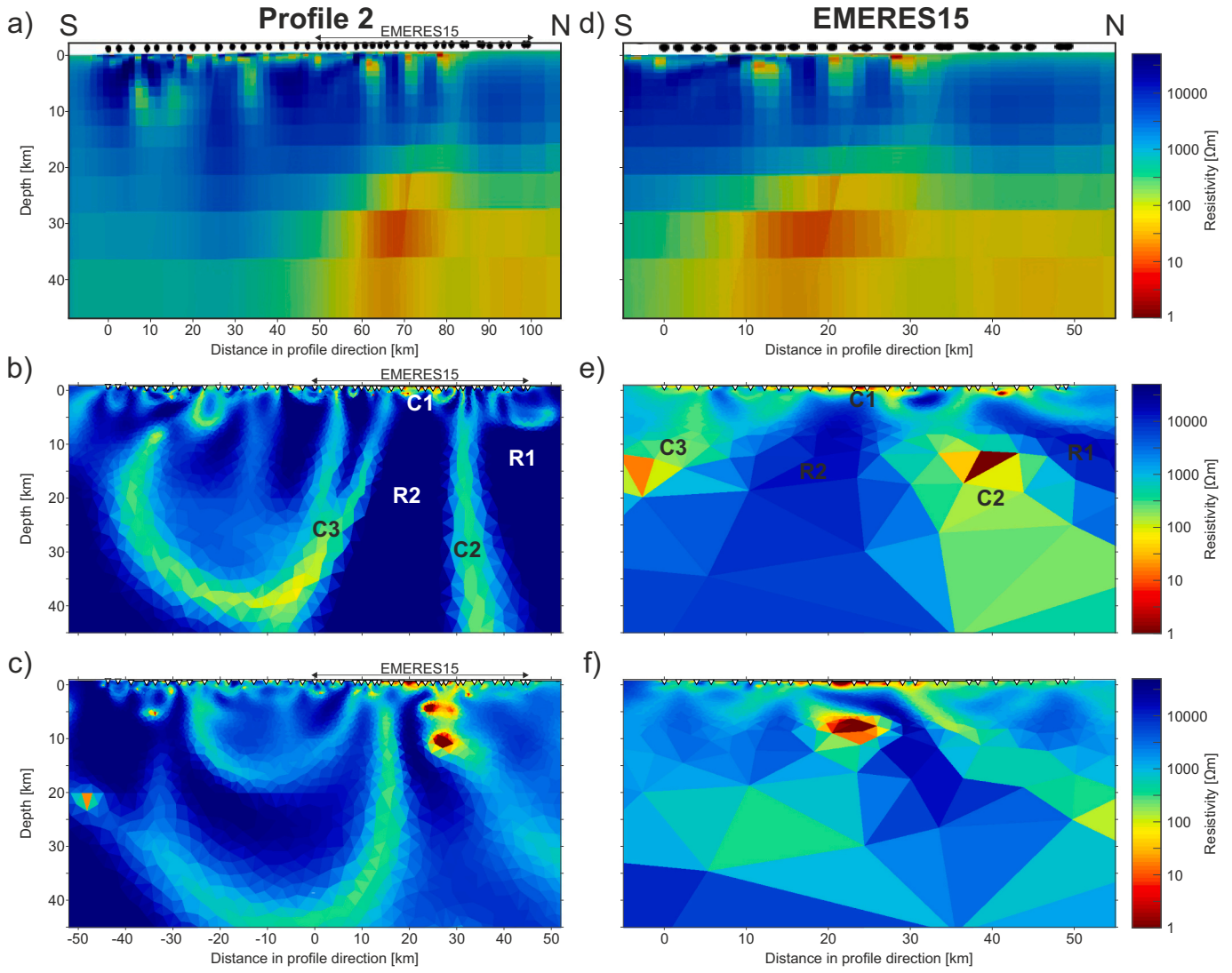

Fig. 12. Two-dimensional sections extracted from the preferred 3D model along profile 2 (a) and the EMERES15 profile (d), 2D inversion results for profile 2 (b) and EMERES15 (e) as well as 2D inversion results of synthetic data obtained from the preferred 3D model for profile 2 (c) and the EMERES15 profile (f) using the same/similar inversion parameters and settings as the corresponding 2D inversion of the real data. All important conductors and resistors interpreted by Muñoz et al. (2018) can be resolved by our 2D models. However, our results clearly demonstrate that the 2D inversion results are significantly affected by off-profile 3D structures. Please note that the colour scale is different to the previous ones.

2, two conductive features are observed in the south (Fig. 12c). One extends down to greater depths and could be associated with the northern branch of C3 observed for the real data inversion (Fig. 12b); the second more shallower conductive feature of the synthetic inversion could be at least partly associated with the southern branch of C3, especially for the more shallower part. This supports our hypothesis, that the southern conductive channel C3 in the 2D inversions of the real data for profile 2 and EMERES15 is also a projection of an off-profile conductor. Due to its spatial proximity and the shape of this conductor with a split into two branches closer to the surface, the conductive channel C3 close to ML resolved in the 3D model is the most probable explanation. This clearly demonstrates that the 2D inversion results are significantly affected by off-profile 3D structures.

Fig. 13 shows a comparison of the 3D result along profile 1 and 3 with the corresponding 2D inversion results of the real data as well as 2D inversion results of synthetic data obtained from the preferred 3D model using the same procedure as described for profile 2.

Shallow, lower resistivities are visible in the northern part of the profile section of the 3D model along profile 1 (Fig. 13a). These resistivities are associated with the sediments of the Cheb Basin and the known degassing centres. Furthermore, parts of the conductor C2, especially its reservoir appears at the northern end of the profile section. In the centre of this 3D excerpt, the resistor R1 is resolved and other small-scale conductors are shown in the middle and southern part of the model belonging to the conductor C4. All these structures are also resolved in the corresponding 2D inversion of the real data (Fig. 13b), although the 2D model appears more complex and the depth, location and inclination of some structures, e.g. the vertical channel of C2, differ from the 3D model. Following the 3D model, the conductor C2 is located north of the stations of profile 1. A possible explanation for its southern inclination in the 2D model is the projection of the stations onto the profile, similar to the observations made by Cruces-Zabala et al. (2020) for their data set. Unfortunately, the conductor C2 is poorly resolved in the 2D model of the synthetic data calculated from the 3D preferred model (Fig. 13c), although a slightly southern inclination is indicated. Nonetheless, this synthetic model shows many similarities with the 2D model of the real data. Especially the conductive anomalies in the south and the shallow, lower resistivities in the northern part can be resolved.

The profile section of the 3D model along profile 3 (Fig. 13d) is dominated by high resistivities of the resistor R1 and some structures

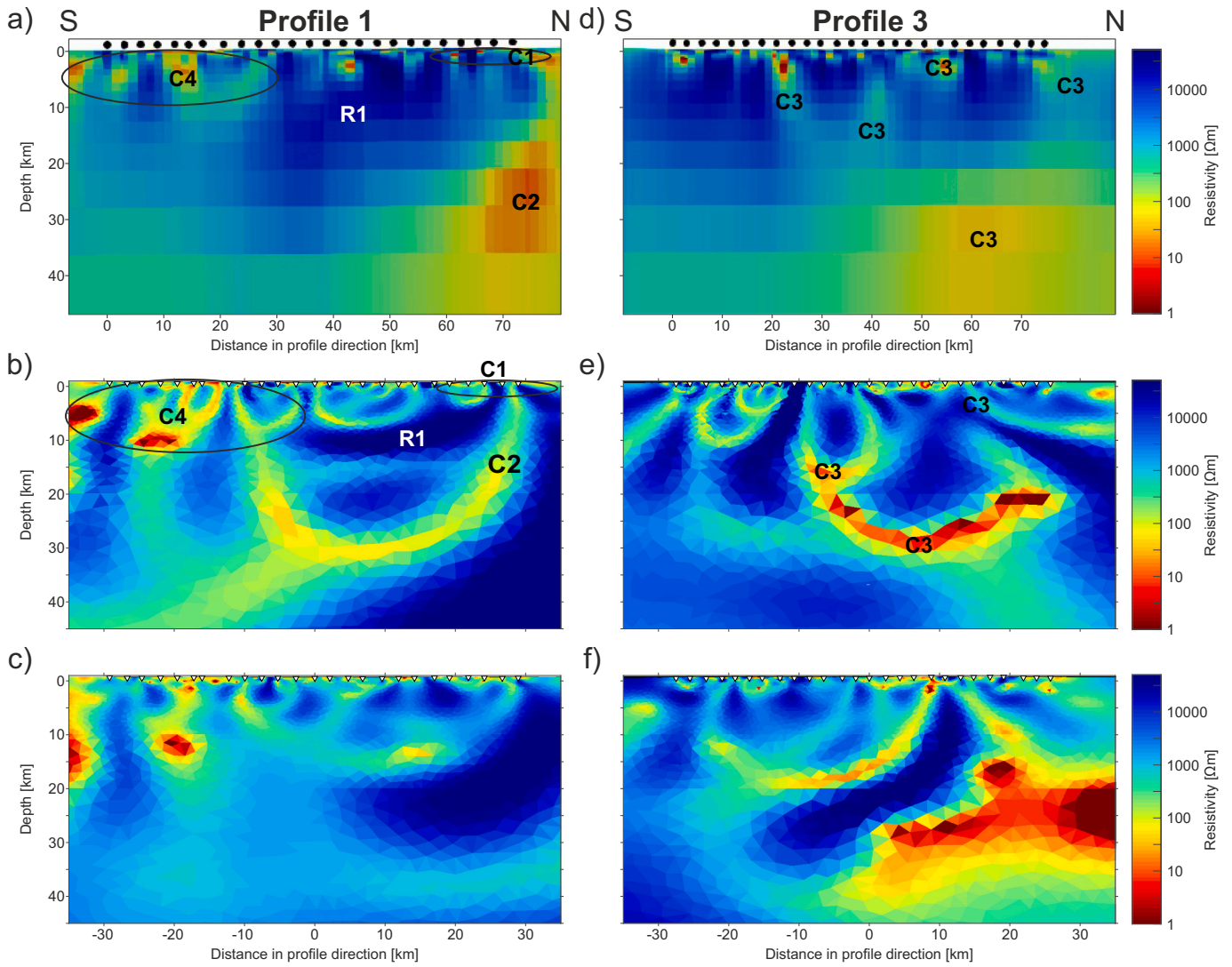

Fig. 13. 3D and 2D inversion results for profile 1 (left column) and profile 3 (right column) presented as sections through the preferred 3D model (a and d), 2D models of the real data (b and e) and 2D models of synthetic data (c and f) calculated from the preferred 3D model. The same colour scale as in Fig. 12 is used.

with lower resistivities associated with the reservoir and different branches of the conductor C3. However, most parts of the conductor C3 are located east of the profile and consequently do not appear in this profile section. The 2D model of the real data (Fig. 13e) shows several conductive structures within a resistive background. The most striking structure is a conductor extending from the centre of the profile up to the north in a depth range of $20 - 30\,km$. Due to its position and depth, this conductor is very likely a projection of the reservoir anomaly C3 resolved in the 3D inversion east of profile 3. Some of the vertical and sub-vertical conductive structures shown in the 2D model can be associated with the different branches of C3, although their inclination and shape differs from the 3D model probably due to their projection. Furthermore, lower resistivities are observed at shallow depths close to ML similar to the 3D model. The 2D inversion result of the synthetic data calculated from the preferred 3D model is shown in Fig. 13f. It also includes a conductive reservoir starting at a depth of $20\,km$ with similar resistivities as observed in the 2D model of the real data. In both cases, the resolved resistivities are much lower than the resistivities observed for this structure in the 3D model. Two conductive branches fork below ML, one dipping to the north and one to the south. They represent very likely the middle branch of C3, that splits close to the surface. Due to the poor data quality of the real data in the vicinity of ML, the appearance and resolution of the different branches of C3 differ in the real and synthetic 2D inversions. However, both 2D models show clearly that 3D features east of the profile considerably influence the 2D inversions.

In general, all 2D inversions of the real and synthetic data showed that the 2D models are significantly affected by 3D and off-profile structures. Some of them are projected into the 2D models. Therefore, a 3D inversion was essential for this data set to determine the true location, shape and conductivities of these structures. Although profile 2 and the previously conducted EMERES15 profile contain the most important anomalies, they were to some extent wrongly positioned leading to incorrect interpretations. For one thing, the conductor C2 is located more to the west. The hypocentres of the swarm earthquakes therefore do not correspond with lower resistivities within this conductor. Instead the hypocentres of the earthquakes cluster around this conductor C2 and are located at the resistive flanks. Furthermore, the conductor C3 in the 2D models of profile 2 and the EMERES15 profile can neither be associated with the Aš-Tachov fault, nor with a suture zone or a conductive feature originating from the Quaternary volcanic structures. Instead, this conductor is very likely a projection of a prominent conductive feature east of the study area that forms a large reservoir at depth and has several ascending channels to the surface feeding for instance the degassing centres around ML.

6. Conclusion

Many of the previous magnetotelluric (MT) field surveys in the study and surrounding area have acquired data either along a few profiles or on small local grids allowing only 2D modelling and rather spatially limited 3D modelling studies. The newly conducted MT data were aligned along three $50 - 75\,km$ long profiles which extend to previous MT stations measured by Muñoz et al. (2018) in the north. Furthermore, additional stations were acquired between the profiles covering the region of the Quaternary volcanic structures, the Aš-Tachov fault and the suture zones of the different tectonic units. Finally, the entire data set consisted of the newly acquired stations, reprocessed stations from the field campaigns in 2015 and 2016 (Muñoz et al., 2018) as well as some stations conducted in the framework of the German Continental Deep Drilling site KTB. These data were utilised to obtain the first comprehensive 3D model of the study area's subsurface electrical resistivity structure. In addition, it allows to determine structures that could not be unambiguous interpreted in previous studies due to either the lack or an unfavourable distribution of stations. Directionality analyses along the individual profile lines show that the geo-electrical strike direction for most of the stations is dominated by the Ohře Rift confirming the findings of Muñoz et al. (2018). Nonetheless, a dimensionality analysis based on beta values of the phase tensors clearly demonstrates that the MT data inherit a strong 3D character especially for longer periods and in some areas for instance close to the mofettes. This indicates that a 2D analysis can resolve the expected complex 3D geo-electrical structure of the subsurface only within certain limits, and underline the necessity of a 3D modelling study.

For the 3D analysis we use the parallelized Modular Electromagnetic Inversion system ModEM (Meqbel, 2009; Egbert and Kelbert, 2012; Kelbert et al., 2014). We conduct several hundreds of inversions testing different parameter settings and strategies. Finally, we use a cascaded inversion to fit the impedance as well as vertical transfer functions. Large parts of the 3D model are dominated by high resistivity values up to $57{,}000\,\Omega m$ representing the crystalline basement of the Variscan tectonic units. Lower resistivities are observed in the west for the units of the Permo-Carboniferous and Mesozoic. Previous measurements in the framework of the German Continental Deep Drilling site already showed that these units have much lower resistivities than the crystalline basement of the Variscan units (Eisel and Haak, 1999; Eisel et al., 2001; Storz et al., 2000). The sedimentary Cheb Basin in the north is resolved down to a depth of approximately $250\,m$ and is characterized by much lower resistivity values. For the near surface, even lower resistivities are observed within the Cheb Basin close to known degassing centres as mofettes or spas. The model reveals a conductive channel beneath the Cheb Basin that extends from the near surface down to the crust-mantle depth forming a conductive reservoir in a depth range of $21 - 28\,km$. This conductive structure resembles the northern conductive channel observed by Muñoz et al. (2018). Furthermore, this conductive structure correlates spatially with the hypocentres of the swarm earthquakes which occurred in the Nový Kostel focal zone between 2000 and 2010. The 3D model also clearly reveals that the hypocentres cluster within the resistive host rock around this conductive structure, comparable to what Becken et al. (2011) observed for the San Andreas Fault. Therefore, our 3D models update and thus contradict the 2D models by Muñoz et al. (2018) in which these hypocentres were located within the conducting deep reaching anomaly. As their profile was located east of the focal zone, they could only use projected locations at that time resulting in this misleading interpretation. Nonetheless, the conductive channel could represent a fluid pathway from the resolved reservoir in the lower crust to the surface feeding e.g. the Bublák and Hartoušov mofette fields, the springs and mofettes within the Soos national nature reserve as well as the spas Františkovy Lázně and Sibyllenbad. Furthermore, the location of this conductive structure coincides with a v_p/v_s anomaly revealed in a seismic tomography study by Mousavi et al. (2015, 2017) that was interpreted by the authors as a mid-crustal solidified igneous body that could be part of a fluid pathway from the mantle up to the surface. Another conductive channel east of the study area is observed in the 3D model. Similar to the conductor in the north, it extends from the surface down to the crust-mantle boundary forming a conductive reservoir at depths of $16 - 21\,km$ depth. Closer to the surface, this conductor forks into several branches. One of them connects to the spa Mariánské Lázně. This conductive feature could be interpreted as another small-scale reservoir at crust-mantle depth and a possible fluid pathway to the surface feeding several degassing spots in the east in the surrounding of Mariánské Lázně. Sensitivity studies confirmed that both conductors can be separated at larger depths supporting the hypothesis of Bräuer et al. (2005, 2008) that the mineral springs at the spas Františkovy Lázně and Mariánské Lázně are supplied by different small-scale spatially separated magmatic reservoirs. However, in the 3D model we could not resolve conductive structures beneath the Quaternary volcanic structures or close to the suture zones of the Variscan units or the Aš-Tachov fault along the profile of Muñoz et al. (2018). This led us to the conclusion that the southern conductor observed in their 2D model has to be very likely a projection of another conductive off-profile structure. Based on the spatial proximity, the conductor east of the study area would be the most obvious explanation for the conductor observed in the previous 2D models. To examine this hypothesis, we compared the 3D model with newly conducted and the previous 2D inversion results as well as conducted synthetic 2D inversions using forward calculated data from the preferred 3D model. A 2D inversion of profile 2 containing both newly conducted stations and the stations used by Muñoz et al. (2018) resolved all interpreted conductive features in their model. Furthermore, the synthetic modelling studies reinforced our hypothesis. Both vertical conductors in the models of Muñoz et al. (2018) are projections of off-profile conductive structures. The northern conductor is located more to the west in the 3D model and the southern conductor in their model is very likely a projection of parts of the conductor east of the current study area. In general, all 2D inversions of the real and synthetic data show that the 2D models are significantly affected by 3D and off-profile structures and confirmed the necessity of the conducted 3D study.

CRediT authorship contribution statement

Anna Platz: Methodology, Formal analysis, Investigation, Visualization, Writing – original draft, Data curation. **Ute Weckmann:** Conceptualization, Project administration, Funding acquisition, Investigation, Writing – review & editing. **Josef Pek:** Resources. **Světlana Kováčiková:** Resources, Investigation, Writing – review & editing. **Radek Klanica:** Resources, Investigation, Writing – review & editing. **Johannes Mair:** Formal analysis, Investigation, Writing – review & editing. **Basel Aleid:** Formal analysis, Investigation, Writing – review & editing.

Declaration of Competing Interest

The authors declare that they have no known competing financial interests or personal relationships that could have appeared to influence the work reported in this paper.

Acknowledgements

The project was funded by the DFG (http://www.dfg.de) with Grant Number WE2938/12-1. The instruments for the field experiment were provided by the Geophysical Instrument Pool Potsdam - GIPP. We greatly appreciate the work of all student and scientific helpers on site and thank all local authorities and landowners for allowing access to the MT sites and for all the support provided. We thank Dr. Johann Rohrmüller (Bayerisches Landesamt für Umwelt) and Danielle Tölg for their support with permitting and logistics. We also like to thank two anonymous reviewers for their constructive comments, which helped to

improve the manuscript.

References

Aivazpourporgou, S., Thiel, S., Hayman, P.C., Moresi, L.N., Heinson, G., 2015. Decompression melting driving intraplate volcanism in Australia: evidence from magnetotelluric sounding. Geophys. Res. Lett. 42, 346–354. https://doi.org/10.1002/2014GL060088.

Aizawa, K., Utsugi, M., Kitamura, K., Koyama, T., Uyeshima, M., Matsushima, N., Takakura, S., Inagaki, H., Saito, H., Fujimitsu, Y., 2021. Magmatic fluid pathways in the upper crust: insights from dense magnetotelluric observations around the Kuju Volcanoes, Japan. Geophys. J. Int. 228, 755–772. https://doi.org/10.1093/gji/ggab368.

Babuška, V., Plomerová, J., 2001. Subcrustal lithosphere around the Saxothuringian–Moldanubian Suture Zone — a model derived from anisotropy of seismic wave velocities. Tectonophysics 332, 185–199. https://doi.org/10.1016/S0040-1951(00)00255-9.

Bai, D., Unsworth, M.J., Meju, M.A., Ma, X., Teng, J., Kong, X., Sun, Y., Sun, J., Wang, L., Jiang, C., et al., 2010. Crustal deformation of the eastern Tibetan plateau revealed by magnetotelluric imaging. Nat. Geosci. 3, 358–362. https://doi.org/10.1038/ngeo830.

Bankwitz, P., Schneider, G., Kämpf, H., Bankwitz, E., 2003. Structural characteristics of epicentral areas in Central Europe: study case Cheb Basin (Czech Republic). J. Geodyn. 35, 5–32. https://doi.org/10.1016/S0264-3707(02)00051-0.

Beccaluva, L., Azzouni-Sekkal, A., Benhallou, A., Bianchini, G., Ellam, R., Marzola, M., Siena, F., Stuart, F., 2007. Intracratonic asthenosphere upwelling and lithosphere rejuvenation beneath the Hoggar swell (Algeria): evidence from HIMU metasomatised lherzolite mantle xenoliths. Earth Planet. Sci. Lett. 260, 482–494. https://doi.org/10.1016/j.epsl.2007.05.047.

Becken, M., Burkhardt, H., 2004. An ellipticity criterion in magnetotelluric tensor analysis. Geophys. J. Int. 159, 69–82. https://doi.org/10.1111/j.1365-246X.2004.02376.x.

Becken, M., Ritter, O., Bedrosian, P.A., Weckmann, U., 2011. Correlation between deep fluids, tremor and creep along the Central San Andreas fault. Nature 480, 87–90. https://doi.org/10.1038/nature10609.

Bräuer, K., Kämpf, H., Strauch, G., Weise, S.M., 2003. Isotopic evidence ($^3He/^4He$,$^{13}C_{CO_2}$) of fluid–triggered intraplate seismicity. J. Geophys. Res. Solid Earth 108. https://doi.org/10.1029/2002JB002077.

Bräuer, K., Kämpf, H., Niedermann, S., Strauch, G., 2005. Evidence for ascending upper mantle–derived melt beneath the Cheb basin, Central Europe. Geophys. Res. Lett. 32 https://doi.org/10.1029/2004GL022205.

Bräuer, K., Kämpf, H., Niedermann, S., Strauch, G., Tesař, J., 2008. Natural laboratory NW Bohemia: Comprehensive fluid studies between 1992 and 2005 used to trace geodynamic processes. Geochem. Geophys. Geosyst. 9 https://doi.org/10.1029/2007GC001921.

Bräuer, K., Kämpf, H., Strauch, G., 2009. Earthquake swarms in non-volcanic regions: what fluids have to say. Geophys. Res. Lett. 36 https://doi.org/10.1029/2009GL039615.

Bräuer, K., Kämpf, H., Strauch, G., 2014. Seismically triggered anomalies in the isotope signatures of mantle–derived gases detected at degassing sites along two neighboring faults in NW Bohemia, Central Europe. J. Geophys. Res. Solid Earth 119, 5613–5632. https://doi.org/10.1002/2014JB011044.

Caldwell, T.G., Bibby, H.M., Brown, C., 2004. The magnetotelluric phase tensor. Geophys. J. Int. 158, 457–469. https://doi.org/10.1111/j.1365-246X.2004.02281.x.

Červ, V., Pek, J., Praus, O., 1997a. The present state of art of long period Magnetotellurics in the Western Part of the Bohemian Massif. J. Geomagn. Geoelectr. 49, 1559–1583. https://doi.org/10.5636/jgg.49.1559.

Červ, V., Pek, J., Praus, O., Zaja, A., Manzella, A., 1997b. Magnetotelluric and deep geomagnetic induction data in the Bohemian Massif. Ann. Geophys. 40 https://doi.org/10.4401/ag-3921.

Červ, V., Kováčiková, S., Pek, J., Pěčová, J., Praus, O., 2001. Geoelectrical structure across the Bohemian Massif and the transition zone to the West Carpathians. Tectonophysics 332, 201–210. https://doi.org/10.1016/S0040-1951(00)00257-2.

Chave, A.D., Jones, A.J., 2012. The Magnetotelluric Method. Cambridge University Press.

Comeau, M.J., Unsworth, M.J., Ticona, F., Sunagua, M., 2015. Magnetotelluric images of magma distribution beneath Volcán Uturuncu, Bolivia: Implications for magma dynamics. Geology 43, 243–246. https://doi.org/10.1130/G36258.1.

Comeau, M.J., Becken, M., Grayver, A.V., Käufl, J.S., Kuvshinov, A.V., 2022. The geophysical signature of a continental intraplate volcanic system: from surface to mantle source. Earth Planet. Sci. Lett. 578, 117307 https://doi.org/10.1016/j.epsl.2021.117307.

Cruces-Zabala, J., Ritter, O., Weckmann, U., Tietze, K., Schmitz, M., 2020. Magnetotelluric imaging of the Mérida Andes and surrounding areas in Venezuela. Geophys. J. Int. 222, 1570–1589. https://doi.org/10.1093/gji/ggaa266.

Dahm, T., Hrubcová, P., Fischer, T., Horálek, J., Korn, M., Buske, S., Wagner, D., 2013. Eger Rift ICDP: an observatory for study of non-volcanic, mid-crustal earthquake swarms and accompanying phenomena. Sci. Drill. 16, 93–99. https://doi.org/10.5194/sd-16-93-2013.

Dahm, T., Anesio, A., Buske, S., Dolejs, D., Horalek, J., Hrubcova, P., Korn, M., Krüger, F., Málek, J., Shelly, D., Wagner, D., 2016. Drilling the Eger Rift: Magmatic Fluids Driving the Earthquake Swarms and the Deep Biosphere: Icdp Proposal Abstract.

DEKORP Research Group, 1987. Results of deep reflection seismic profiling in the Oberpfalz (Bavaria). Geophys. J. Int. 89, 353–360. https://doi.org/10.1111/j.1365-246X.1987.tb04430.x.

Dèzes, P., Schmid, S., Ziegler, P., 2004. Evolution of the European Cenozoic Rift System: interaction of the Alpine and Pyrenean orogens with their foreland lithosphere. Tectonophysics 389, 1–33. https://doi.org/10.1016/j.tecto.2004.06.011.

Di Mauro, D., Volpi, G., Manzella, A., Zaja, A., Praticelli, N., Červ, V., Pek, J., De Santis, A., 1999. Magnetotelluric investigations of the seismically active region of Northwest Bohemia: preliminary results. Ann. Geophys. 42 https://doi.org/10.4401/ag-3698.

Egbert, G.D., Kelbert, A., 2012. Computational recipes for electromagnetic inverse problems. Geophys. J. Int. 189, 251–267. https://doi.org/10.1111/j.1365-246X.2011.05347.x.

Eisel, M., Haak, V., 1999. Macro-anisotropy of the electrical conductivity of the crust: a magnetotelluric study of the german continental deep drilling site (ktb). Geophys. J. Int. 136, 109–122. https://doi.org/10.1046/j.1365-246X.1999.00707.x.

Eisel, M., Haak, V., Pek, J., Červ, V., 2001. A magnetotelluric profile across the German Deep Drilling Project (KTB) area: Two– and three–dimensional modeling results. J. Geophys. Res. Solid Earth 106, 16061–16073. https://doi.org/10.1029/2000JB900451.

Emmermann, R., Lauterjung, J., 1997. The german continental deep drilling program ktb: overview and major results. J. Geophys. Res. Solid Earth 102, 18179–18201. https://doi.org/10.1029/96JB03945.

Enderle, U., Schuster, K., Prodehl, C., Schulze, A., Bribach, J., 1998. The refraction seismic experiment GRANU95 in the Saxothuringian belt, southeastern Germany. Geophys. J. Int. 133, 245–259. https://doi.org/10.1046/j.1365-246X.1998.00462.x.

Fischer, T., Horálek, J., Hrubcová, P., Vavryčuk, V., Bräuer, K., Kämpf, H., 2014. Intra-continental earthquake swarms in West-Bohemia and Vogtland: a review. Tectonophysics 611, 1–27. https://doi.org/10.1016/j.tecto.2013.11.001.

Flechsig, C., Bussert, R., Rechner, J., Schütze, C., Kämpf, H., 2008. The Hartousov Mofette Field in the Cheb Basin, Western Eger Rift (Czech republic): a Comperative Geoelectric, Sedimentologic and Soil Gas Study of a Magmatic Diffuse CO_2-degassing Structure. Z. Geol. Wiss. 36, 177–193.

Flechsig, C., Heinicke, J., Mrlina, J., Kämpf, H., Nickschick, T., Schmidt, A., Bayer, T., Günther, T., Rücker, C., Seidel, E., Seidl, M., 2015. Integrated geophysical and geological methods to investigate the inner and outer structures of the Quaternary Mýtina maar (W-Bohemia, Czech Republic). Int. J. Earth Sci. 104, 2087–2105. https://doi.org/10.1007/s00531-014-1136-0.

Gao, J., Zhang, H., Zhang, S., Xin, H., Li, Z., Tian, W., Bao, F., Cheng, Z., Jia, X., Fu, L., 2020. Magma recharging beneath the Weishan volcano of the intraplate Wudalianchi volcanic field, Northeast China, implied from 3-D magnetotelluric imaging. Geology 48, 913–918. https://doi.org/10.1130/G47531.1.

Geissler, W.H., Kämpf, H., Kind, R., Bräuer, K., Klinge, K., Plenefisch, T., Horálek, J., Zedník, J., Nehybka, V., 2005. Seismic structure and location of a CO_2 source in the upper mantle of the western Eger (Ohře) Rift, Central Europe. Tectonics 24. https://doi.org/10.1029/2004TC001672.

Geissler, W.H., Kämpf, H., Seifert, W., Dulski, P., 2007. Petrological and seismic studies of the lithosphere in the earthquake swarm region Vogtland/NW Bohemia, Central Europe. J. Volcanol. Geotherm. Res. 159, 33–69. https://doi.org/10.1016/j.jvolgeores.2006.06.011.

Grad, M., Guterch, A., Mazur, S., Keller, G.R., Špičák, A., Hrubcová, P., Geissler, W.H., 2008. Lithospheric structure of the Bohemian Massif and adjacent Variscan belt in Central Europe based on profile S01 from the SUDETES 2003 experiment. J. Geophys. Res. Solid Earth 113. https://doi.org/10.1029/2007JB005497.

Grygar, R., 2016. Geology and tectonic development of the czech republic. In: Pánek, T., Hradecký, J. (Eds.), Landscapes and Landforms of the Czech Republic. Springer, Cham. https://doi.org/10.1007/978-3-319-27537-6_2. World geomorphological landscapes.

Haak, V., Hutton, R., 1986. Electrical resistivity in continental lower crust. Geol. Soc. Lond., Spec. Publ. 24, 35–49. https://doi.org/10.1144/GSL.SP.1986.024.01.05.

Heuer, B., Geissler, W.H., Kind, R., Kämpf, H., 2006. Seismic evidence for asthenospheric updoming beneath the western Bohemian Massif, Central Europe. Geophys. Res. Lett. 33 https://doi.org/10.1029/2005GL025158.

Horálek, J., Fischer, T., 2009. Role of crustal fluids in triggering the West Bohemia/Vogtland earthquake swarms: just what we know (a review). Stud. Geophys. Geod. 52, 455. https://doi.org/10.1007/s11200-008-0032-0.

Hošek, J., Valenta, J., Rapprich, V., Hroch, T., Turjaková, V., Tábořík, P., Pokorný, P., 2019. Newly identified Pleistocene maars in Western Bohemia (Czech Republic). Geosci. Res. Rep. 52, 97–104. https://doi.org/10.3140/zpravy.geol.2019.23.

Hrubcová, P., Środa, P., Špičák, A., Guterch, A., Grad, M., Keller, G.R., Brueckl, E., Thybo, H., 2005. Crustal and uppermost mantle structure of the Bohemian Massif based on CELEBRATION 2000 data. J. Geophys. Res. Solid Earth 110. https://doi.org/10.1029/2004JB003080.

Hrubcová, P., Vavryčuk, V., Boušková, A., Horálek, J., 2013. Moho depth determination from waveforms of microearthquakes in the West Bohemia/Vogtland swarm area. J. Geophys. Res. Solid Earth 118, 120–137. https://doi.org/10.1029/2012JB009360.

Hrubcová, P., Geissler, W.H., Bräuer, K., Vavryčuk, V., Tomek, Č., Kämpf, H., 2017. Active magmatic underplating in Western Eger Rift, Central Europe. Tectonics 36, 2846–2862. https://doi.org/10.1002/2017TC004710.

Jarchow, C.M., Thompson, G.A., Catchings, R.D., Mooney, W.D., 1993. Seismic evidence for active magmatic underplating beneath the Basin and Range Province, western United States. J. Geophys. Res. Solid Earth 98, 22095–22108. https://doi.org/10.1029/93JB02021.

Kämpf, H., Bräuer, K., Schumann, J., Hahne, K., Strauch, G., 2013. CO_2 discharge in an active, non-volcanic continental rift area (Czech Republic): Characterisation ($\delta^{13}C$, $^3He/^4He$) and quantification of diffuse and vent CO_2 emissions. Chem. Geol. 339, 71–83. https://doi.org/10.1016/j.chemgeo.2012.08.005.

Kelbert, A., Meqbel, N., Egbert, G.D., Tandon, K., 2014. ModEM: a modular system for inversion of electromagnetic geophysical data. Comput. Geosci. 66, 40–53. https://doi.org/10.1016/j.cageo.2014.01.010.

Key, K., 2016. MARE2DEM: a 2-D inversion code for controlled-source electromagnetic and magnetotelluric data. Geophys. J. Int. 207, 571–588. https://doi.org/10.1093/gji/ggw290.

Key, K., Ovall, J., 2011. A parallel goal-oriented adaptive finite element method for 2.5-D electromagnetic modelling. Geophys. J. Int. 186, 137–154. https://doi.org/10.1111/j.1365-246X.2011.05025.x.

Krings, T., 2007. The Influence of Robust Statistics, Remote Reference, and Horizontal Magnetic Transfer Functions on Data Processing in Magnetotellurics. Diploma thesis. Westfälische Wilhelms-Universität Münster. Münster.

Kütter, S., Weckmann, U., de Wit, M., 2016. A deep electrical conductivity structure of the southern Barberton Greenstone Belt, South Africa, derived from magnetotelluric measurements. S. Afr. J. Geol. 119, 273–290. https://doi.org/10.2113/gssajg.119.1.273.

Mair, J., 2020. Interpretation of MT Data in the Eger Rift along the Regional Profiles. Master thesis. Freie Universität Berlin, Berlin.

Matte, P., Maluski, H., Rajlich, P., Franke, W., 1990. Terrane boundaries in the Bohemian Massif: result of large-scale Variscan shearing. Tectonophysics 177, 151–170. https://doi.org/10.1016/0040-1951(90)90279-H.

Meqbel, N., 2009. The Electrical Conductivity Structure of the Dead Sea Basin Derived from 2D and 3D Inversion of Magnetotelluric Data. Phd thesis. Freie Universität Berlin, Berlin.

Meqbel, N., Weckmann, U., Muñoz, G., Ritter, O., 2016. Crustal metamorphic fluid flux beneath the Dead Sea Basin: constraints from 2-D and 3-D magnetotelluric modelling. Geophys. J. Int. 207, 1609–1629. https://doi.org/10.1093/gji/ggw359.

Mousavi, S., Bauer, K., Korn, M., Hejrani, B., 2015. Seismic tomography reveals a mid-crustal intrusive body, fluid pathways and their relation to the earthquake swarms in West Bohemia/Vogtland. Geophys. J. Int. 203, 1113–1127. https://doi.org/10.1093/gji/ggv338.

Mousavi, S., Haberland, C., Bauer, K., Hejrani, B., Korn, M., 2017. Attenuation tomography in West Bohemia/Vogtland. Tectonophysics 695, 64–75. https://doi.org/10.1016/j.tecto.2016.12.010.

Mrlina, J., Kämpf, H., Kroner, C., Mingram, J., Stebich, M., Brauer, A., Geissler, W.H., Kallmeyer, J., Matthes, H., Seidl, M., 2009. Discovery of the first Quaternary maar in the Bohemian Massif, Central Europe, based on combined geophysical and geological surveys. J. Volcanol. Geotherm. Res. 182, 97–112. https://doi.org/10.1016/j.jvolgeores.2009.01.027.

Mrlina, J., Kämpf, H., Polák, V., Seidl, M., 2019. Indikace dvou neznámých kvartérních maarových vulkánů u Libé v západních Čechách na základě gravimetrického průzkumu. Zpravodaj Hnědé uhlí 19–23.

Mullick, N., Buske, S., Hrubcova, P., Ruzek, B., Shapiro, S., Wigger, P., Fischer, T., 2015. Seismic imaging of the geodynamic activity at the western Eger rift in Central Europe. Tectonophysics 647-648, 105–111. https://doi.org/10.1016/j.tecto.2015.02.010.

Muñoz, G., Weckmann, U., Pek, J., Kováčiková, S., Klanica, R., 2018. Regional two-dimensional magnetotelluric profile in West Bohemia/Vogtland reveals deep conductive channel into the earthquake swarm region. Tectonophysics 727, 1–11. https://doi.org/10.1016/j.tecto.2018.01.012.

Nickschick, T., Kämpf, H., Flechsig, C., Mrlina, J., Heinicke, J., 2015. CO_2 degassing in the Hartoušov mofette area, western Eger Rift, imaged by CO_2 mapping and geoelectrical and gravity surveys. Int. J. Earth Sci. 104, 2107–2129. https://doi.org/10.1007/s00531-014-1140-4.

Nickschick, T., Flechsig, C., Mrlina, J., Oppermann, F., Löbig, F., Günther, T., 2019. Large-scale electrical resistivity tomography in the Cheb Basin (Eger Rift) at an International Continental Drilling Program (ICDP) monitoring site to image fluid-related structures. Solid Earth 10, 1951–1969. https://doi.org/10.5194/se-10-1951-2019.

Oettinger, G., Haak, V., Larsen, J.C., 2001. Noise reduction in magnetotelluric time-series with a new signal–noise separation method and its application to a field experiment in the Saxonian Granulite Massif. Geophys. J. Int. 146, 659–669. https://doi.org/10.1046/j.1365-246X.2001.00473.x.

Ogawa, Y., Mishina, M., Goto, T., Satoh, H., Oshiman, N., Kasaya, T., Takahashi, Y., Nishitani, T., Sakanaka, S., Uyeshima, M., Takahashi, Y., Honkura, Y., Matsushima, M., 2001. Magnetotelluric imaging of fluids in intraplate earthquake zones, NE Japan back arc. Geophys. Res. Lett. 28, 3741–3744. https://doi.org/10.1029/2001GL013269.

Ogawa, Y., Ichiki, M., Kanda, W., Mishina, M., Asamori, K., 2014. Three-dimensional magnetotelluric imaging of crustal fluids and seismicity around Naruko volcano, NE Japan. Earth Planets Space 66, 1–13.

Platz, A., Weckmann, U., 2019. An automated new pre-selection tool for noisy Magnetotelluric data using the Mahalanobis distance and magnetic field constraints. Geophys. J. Int. 218, 1853–1872. https://doi.org/10.1093/gji/ggz197.

Plomerová, J., Munzarová, H., Vecsey, L., Kissling, E., Achauer, U., Babuška, V., 2016. Cenozoic volcanism in the Bohemian Massif in the context of P– and S–velocity high–resolution teleseismic tomography of the upper mantle. Geochem. Geophys. Geosyst. 17, 3326–3349. https://doi.org/10.1002/2016GC006318.

Prodehl, C., Mueller, S., Haak, V., 1995. Continental rifts: evolution, structure, tectonics. In: Continental Rifts: Evolution, Structure, Tectonics. KH Olsen, New York, pp. 133–212.

Prodehl, C., Mueller, S., Haak, V., 2006. The european cenozoic rift system. In: Olsen, K. (Ed.), Developments in Geotectonics : Continental Rifts:Evolution, Structure, Tectonics, vol. 25. Elsevier, pp. 133–212. https://doi.org/10.1016/S0419-0254(06)80012-1.

Ritter, O., Junge, A., Dawes, G.J., 1998. New equipment and processing for magnetotelluric remote reference observations. Geophys. J. Int. 132, 535–548. https://doi.org/10.1046/j.1365-246X.1998.00440.x.

Ritter, O., Muñoz, G., Weckmann, U., Klose, R., Rulff, P., Rettig, S., Müller-Brettschneider, C., Schüler, M., Willkommen, G., Eydam, D., 2015. A Permanent Magnetotelluric Remote Reference Station in Wittstock, Germany. https://doi.org/10.2312/GFZ.B103-15092.

Rohrmüller, J., Kämpf, H., Geiß, E., Großmann, J., Grun, I., Mingram, J., Mrlina, J., Plessen, B., Stebich, M., Veress, C., Wendt, A., Nowaczyk, N., 2018. Reconnaissance study of an inferred Quaternary maar structure in the western part of the Bohemian Massif near Neualbenreuth, NE-Bavaria (Germany). Int. J. Earth Sci. 107, 1381–1405. https://doi.org/10.1007/s00531-017-1543-0.

Rulff, P., Weckmann, U., Kalscheuer, T., Willkommen, G., Buntin, L., 2021. Imaging Mofette Structures in the Ohře (Eger) Rift System, Czech Republic, with Radio-Magnetotelluric Data Using Different Inversion Algorithms. Near Surface Geophysics submitted.

Simpson, F., Bahr, K., 2005. Practical Magnetotellurics, 1. publ ed. Cambridge Univ. Press, Cambridge.

Storz, J., Storz, W., Jacobs, F., 2000. Electrical resistivity tomography to investigate geological structures of the earth's upper crust. Geophys. Prospect. 48, 455–471. https://doi.org/10.1046/j.1365-2478.2000.00196.x.

Ulrych, J., Dostal, J., Adamovič, J., Jelínek, E., Špaček, P., Hegner, E., Balogh, K., 2011. Recurrent Cenozoic volcanic activity in the Bohemian Massif (Czech Republic). Lithos 123, 133–144. https://doi.org/10.1016/j.lithos.2010.12.008.

Unsworth, M., Jones, A.G., Wei, W., Marquis, G.L., Gokarn, S.G., Spratt, J., 2005. Crustal rheology of the Himalaya and Southern Tibet inferred from magnetotelluric data. Nature 438, 78–81. https://doi.org/10.1038/nature04154.

Weckmann, U., Platz, A., 2020. Site Characterization of the PIER-ICDP Drill Holes by Imaging the Subsurface Electrical Conductivity Structure: Local and Regional Structure Beneath Mýtina and Neualbenreuth Maar (ConeEM). https://doi.org/10.5880/GIPP-MT.201810.1.

Weckmann, U., Magunia, A., Ritter, O., 2005. Effective noise separation for magnetotelluric single site data processing using a frequency domain selection scheme. Geophys. J. Int. 161, 635–652. https://doi.org/10.1111/j.1365-246X.2005.02621.x.

Weinlich, F.H., 2014. Carbon dioxide controlled earthquake distribution pattern in the NW Bohemian swarm earthquake region, western Eger Rift, Czech Republic – gas migration in the crystalline basement. Geofluids 14, 143–159. https://doi.org/10.1111/gfl.12058.

Weinlich, F.H., Tesař, J., Weise, S.M., Bräuer, K., Kämpf, H., 1998. Gas flux distribution in mineral springs and tectonic structure in the western Eger Rift. J. Czech Geol. Soc. 43, 91–110.

Weinlich, F.H., Stejskal, V., Teschner, M., Poggenburg, J., 2013. Geodynamic processes in the NW Bohemian swarm earthquake region, Czech Republic, identified by continuous gas monitoring. Geofluids 13, 305–330. https://doi.org/10.1111/gfl.12027.

Wiese, H., 1962. Geomagnetische Tiefentellurik Teil II: Die Streichrichtung der untergrundstrukturen des elektrischen Widerstandes, erschlossen aus geomagnetischen Variationen. Geofisica Pura Appl. 52, 83–103. https://doi.org/10.1007/BF01996002.

Ziegler, P.A., 1992. European Cenozoic rift system. Tectonophysics 208, 91–111. https://doi.org/10.1016/0040-1951(92)90338-7.